BIOPHYSICAL CHARACTERIZATION OF SECRETORY VESICLE TETHERS

A Dissertation

Presented to the Faculty of the Graduate School

of Cornell University

In Partial Fulfillment of the Requirements for the Degree of

Doctor of Philosophy

by

Mark Christopher Harris

August 2014

BIOPHYSICAL CHARACTERIZATION OF SECRETORY VESICLE TETHERS

Mark Christopher Harris, Ph.D.

Cornell University 2014

Although exocytosis has been widely studied, much remains to be discovered. In particular, the identities and mechanical properties of the tether that links a secretory vesicle to the target membrane during the tethering phase of exocytosis are not known. A method to measure vesicle-vesicle tethering interactions with a dual optical trap was modified to detect vesicle-vesicle fusion via dye transfer. Vesicles were loaded with a fluorescent label and allowed to bind. The fluorescence intensity per vesicle volume was measured, but showed no conclusive evidence of dye transfer.

A novel method was developed to measure nanomechanical properties of secretory vesicle-plasma membrane tethers by combined AFM force clamp and TIRF microscopy on membrane sheets from PC12 cells expressing the vesicle marker ANF-eGFP. Tether extensions were composed of multiple steps with variable length. Tethers were more easily unfolded in the presence of GTPγS, as indicated by a higher frequency of short tether extension events. A mean length for the short extension events of ~7 nm was identified, consistent with extension lengths expected from unfolding of a single alpha helix of the exocyst complex. The frequency of these extension events was markedly increased when a fluorescent vesicle was identified at the cantilever tip, indicating that the method reveals specifically the biomechanical properties of physiological vesicle-plasma membrane tethers. The stepwise tether extension events observed with this method are consistent with progressive unfolding

of helical domains of the exocyst complex. This is a highly versatile method that paves the way for future experiments on the mechanical and regulatory properties of secretory vesicle-plasma membrane tethers.

BIOGRAPHICAL SKETCH

Mark was born in Twin Falls, Idaho, and was the third of four children. During his childhood, he lived in Idaho, Montana, Oklahoma, and finally North Carolina, where he attended the North Carolina School of Science and Mathematics, which was a transformative experience. Driven by a desire to understand the world on a fundamental level, he received bachelor's degrees in Physics and Applied Mathematics at North Carolina State University. He joined the PhD program in Applied Physics at Cornell in 2004, where he joined Dr. Manfred Lindau's lab to study the biophysics of secretory vesicle tethering.

Dedicated to my loving and supportive family.

To my father Gene, who helped me through the tough times.

To my mother Carol, who nurtured a family.

To my sister Melinda, who exemplifies compassion and strength of identity.

To my brother Michael, who has shown the power of determination.

To my sister Kathleen, who inspires me to make my life a work of art.

ACKNOWLEDGMENTS

I am indebted to many people who have been a part of the long education leading up to this thesis. I have been a student of many teachers throughout my life that taught and encouraged me along this path. I especially appreciate the patient teachers at Undercroft Montessori School in Tulsa and the teachers at the North Carolina School of Science and Mathematics who challenged me.

I thank Prof. Manfred Lindau for inviting me to work in his lab, and for providing me with great responsibility for very challenging projects. Joan Lenz trained me in isolation of eosinophils and provided me with many PC12 cell samples. I had helpful discussions with many Lindau lab members over the years, including Ray Molloy, Kassandra Kisler Elliott, Brian Kim, and Joannalyn Delacruz. My committee members, Barbara Baird and Chris Xu, provided me with guidance and alternate points of view.

Christopher Umbach provided me with invaluable training and collaboration in the development of my experiments, along with much appreciated support and advice. Teresa Porri, Brian Bowman, and Carol Bayles trained me in the use of equipment, and frequently helped me troubleshoot problems with it. James Inman helped me align the optical trap.

Finally, my family supported me through the challenges of this undertaking.

TABLE OF CONTENTS

LIST OF FIGURES

LIST OF TABLES

CHAPTER 1

EXOCYTOSIS AND TETHERING

1.1 Introduction

Regulated exocytosis is used by many cells to release molecules that cannot pass through the cell membrane directly. Secretory vesicles containing the molecules to be released fuse with the cell membrane, thereby releasing their contents into the cytosol. Material is stored in these vesicles (also called dense core granules) in a dense core that is osmotically inert and promotes efficient storage of molecules[1,2]. Many important processes in the body rely on cells specialized for the release of specific molecules by regulated exocytosis. Examples of this include nerve signal transmission, which relies on neurotransmitter release by neurons, release of hormones, such as epinephrine from chromaffin cells, and release of cytotoxic proteins from eosinophils in the immune response. Secretory vesicle fusion with the plasma membrane is preceded by several steps that confer targeting specificity to the fusion site and lead up to the final assembly of the fusion machinery[3]. In the earliest stages of vesicle association with the plasma membrane, the vesicle is in a tethered state, in which the vesicle is attached to the membrane by a link > 25 nm long[4]. Although several proteins have been implicated in tethering, the specific proteins that make up the tether are unknown. In this chapter, I will discuss the stages of exocytosis and the proteins known to be involved in tethering before providing a preview of the upcoming chapters.

1.2 The SNARE Complex

Any discussion of exocytosis must begin with the Soluble N-ethylmaleimide sensitive factor (NSF) Attachment Protein Receptors (SNAREs) complex, a family of proteins that mediates membrane fusion in the cell, the discovery of which earned Dr. James Rothman a share of the 2013 Nobel Prize in Physiology or Medicine for discoveries of the machinery regulating cell traffic[5]. The SNARE complex alone is sufficient for membrane fusion[3,6], and the complete formation of the SNARE complex is the final step preceding fusion in exocytosis. The core SNARE complex consists of the proteins VAMP/synaptobrevin in the vesicle membrane, and syntaxin I and SNAP-25 in the target plasma membrane[1]. These proteins are thought to form a trans-SNARE complex that holds the membranes together and induces fusion[3], although the existence of a stable trans-SNARE state is still a matter of debate[7].

1.3 Stages of Vesicle Association with the Target Plasma Membrane

Although the SNARE complex is highly involved in the final stages of exocytosis, vesicle association with the plasma membrane precedes assembly of the SNARE complex[8]. Vesicle-plasma membrane fusion is preceded by tethering, in which the vesicle is associated with the plasma membrane via an extended tether (Fig. 1.1). Multiple observations affirm the existence of the tethered state preceding SNARE involvement. On some membranes, vesicles fuse only to localized regions, even though SNAREs are widely distributed on those membranes[9]. Cleavage of squid synaptic SNAREs with toxins results in more synaptic vesicles associated with the plasma membrane, rather than fewer vesicles[9]. When the SNARE protein VAMP is

cleaved, neurosecretory vesicles accumulate at the synapse, indicating that the SNARE complex functions after vesicle association with the plasma membrane is already established[1]. Finally, in chromaffin cells, vesicles newly associated with the membrane continue to move as if held by a 70 nm tether[10], and this motion is not dependent on intact SybII or SNAP-25[11].

The tethered state is followed by docking and priming, and finally fusion. The precise distinction between these steps has not been clear and consistent in the literature, due in part to limitations of electron microscopic studies[1]. One suggestion is that the vesicle and target membrane are held together within >25 nm in the tethered state, and 5 – 10 nm in the docked state[4]. Additionally, the docked state is widely thought to involve trans-pairing of SNAREs[12,13], which can only begin to form when the vesicle-plasma membrane distance is below 8 nm[14]. The SNARE proteins in the vesicle and plasma membrane form a coiled coil, and unzippering of the SNARE complex using optical tweezers results in ~8.3 nm extension[15]. Therefore, docking can be considered to be a state that involves trans-pairing of SNAREs, while tethering precedes trans-pairing of SNAREs. The primed state is thought to involve partial SNARE complex assembly[3] and making the vesicle readily releasable[1]. It has been suggested that vesicles associated with the plasma membrane by multiple tethers < 5 nm are primed[16].

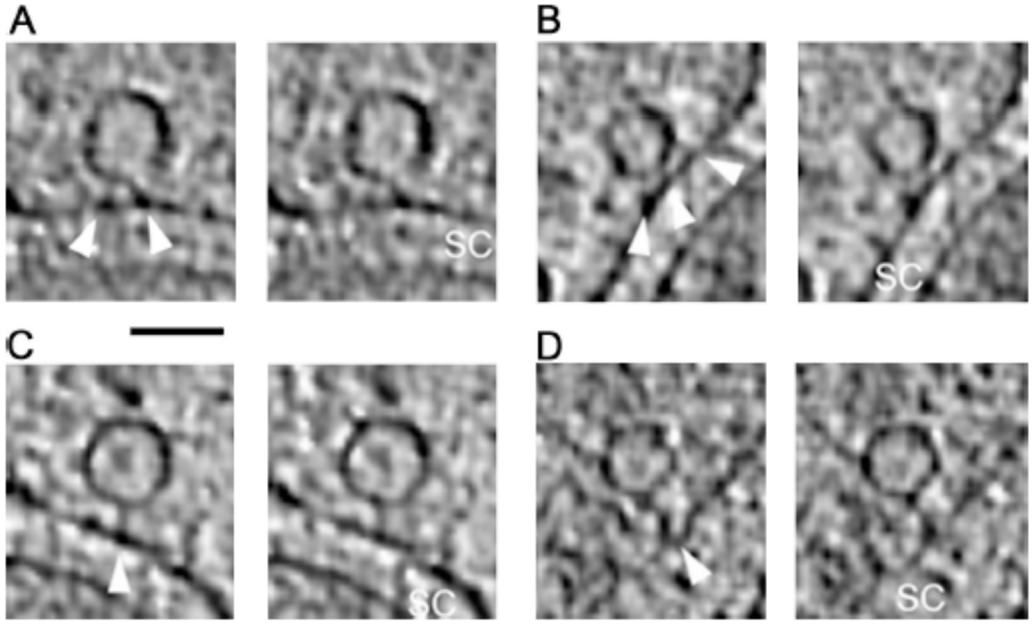

Figure 1.1. Synaptic vesicle tethers. Panels A and B show tethers < 5 nm long, while panels C and D show tethers > 5 nm long (white arrows). Bar is 50 nm. Image from Fernández-Busnadiego, R. *et al.* Quantitative analysis of the native presynaptic cytomatrix by cryoelectron tomography. *J. Cell Biol.* **188,** 145–156 (2010).

1.4 Proteins Implicated in Exocytosis and Tethering

Multiple protein complexes have been implicated in exocytosis. Among them are long coiled-coil proteins and multi-subunit tethering complexes (MTCs)[3]. Many MTCs contain CATCHR (Complex Associated with Tethering Containing Helical Rods) domains, characterized by an extended rod-like structure composed of helical bundles[3,17]. These CATCHR domains promote an elongated structure and mediate interactions with other proteins, such as GTPases. Among the CATCHR proteins that have been implicated in exocytosis are the exocyst complex, Conserved Oligomeric Golgi (COG) complex, Dsl1 complex, Golgi-associated Retrograde Protein (GARP) complex, Calcium-dependent Activator Protein for Secretion (CAPS), Munc13, and

the class V myosin Myo2. The HOPS (Homotypic Fusion and Vacuole Protein Sorting) complex, which likely provides the tethering required for homotypic fusion between large organelles, lacks CATCHR domains. Compound exocytosis, a process in which multiple secretory vesicles fuse to each other within the cell before releasing their contents through a single fusion pore[18], is an example of homotypic fusion.

The exocyst complex consists of 8 subunits: Sec3, Sec5, Sec6, Sec8, Sec10, Sec15, Exo70, and Exo84[3]. Most of the subunits were first identified in yeast[19], but the Exo84 subunit was only identified later in PC12 cells[20]. The exocyst complex has been shown to function after neurosecretory vesicles have been delivered to exocytic sites, but prior to formation of SNARE complexes[8], which suggests a role of the exocyst during the tethering phase of exocytosis. The exocyst complex also determines when and where vesicles are tethered[8]. Finally, Exo70 and Sec3 are associated with the plasma membrane, and Sec3 is localized to exocytic sites[21], while the remaining subunits are bound to the vesicle. These findings have led to the hypothesis that assembly of the full complex could form the physical tether[3,22].

1.5 GTP-Binding Proteins Are Key in Regulation of Tethering

Many GTP-binding proteins, such as members of the Rab family, have also been implicated in tethering[3], and in particular in the function of the exocyst (Fig. 1.2). The GTP-binding protein sec4p, which is present on secretory vesicles[9], is required for the exocyst complex to fully assemble[23]. Subunit Sec15p binds preferentially to the GTP-bound form of sec4p[23]. When the mammalian ortholog of sec4p, Rab3a[24], is locked in either the GTP-bound or the GDP-bound state in chromaffin cells, the

number of vesicles within 100 nm of the plasma membrane decreases, while the number of vesicles found at distances >100 nm from the membrane is not affected[25]. Additionally, interactions of Exo70 and Sec3 with GTPases from the Rho and cdc42 family are involved in recruitment of the exocyst complex to the plasma membrane[3], the GTP-bound form of Ral binds to Sec5p[26], and TC10 binds preferentially to the GTP-bound form of TC10[27].

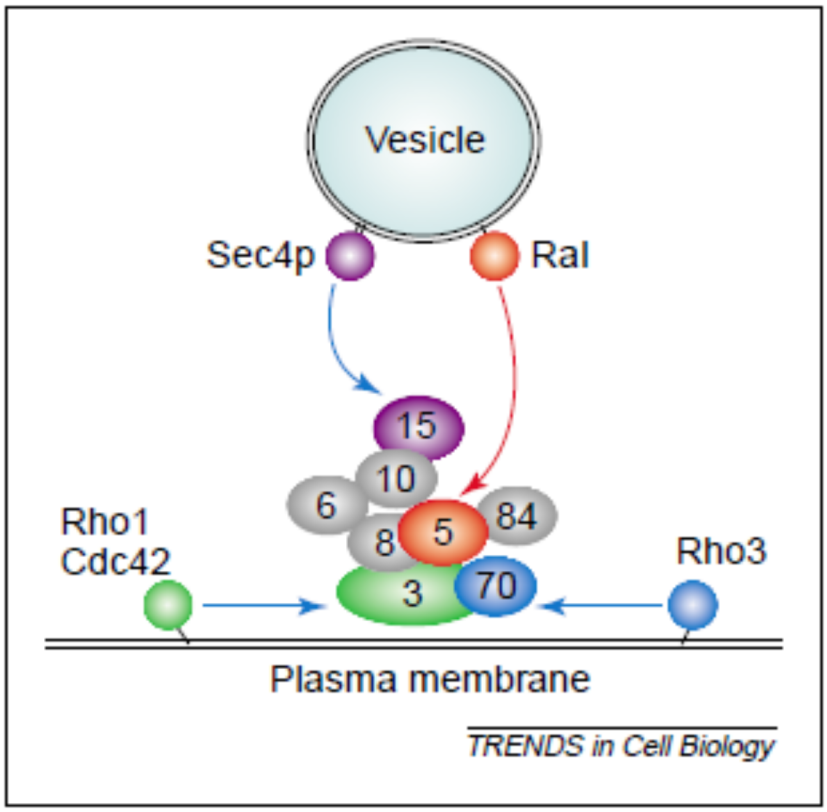

Figure 1.2. Diagram of the interactions of the exocyst with GTP binding proteins. Image from Novick, P. & Guo, W. Ras family therapy: Rab, Rho and Ral talk to the exocyst. *Trends Cell Biol.* **12,** 247–249 (2002).

1.6 Overview of Upcoming Chapters

Although many proteins have been implicated in the process of secretory vesicle tethering, the proteins that make up the physical tether are not known[28]. In this work, methods of directly applying forces to tethers are developed to provide information about their mechanical properties, with the goal of discovering the identities of the proteins that form the tether.

Chapter 2 describes the central methods used in the present work: optical trapping, atomic force microscopy (AFM), and total internal reflection fluorescence microscopy, followed by an introduction to the literature on pulling experiments on proteins and the new methods developed in this work.

In chapter 3, previous vesicle-vesicle pulling experiments using a dual optical trap[29] are enhanced by loading vesicles with fluorescent markers to test for vesicle-vesicle fusion, as has been observed during compound exocytosis[18].

In chapter 4, a method is developed to apply pulling forces directly to secretory vesicle-plasma membrane tethers using a combined AFM/TIRF assembly, allowing direct characterization of the mechanical and regulatory properties of the physical tethers.

In chapter 5, the method developed in chapter 4 is used to measure secretory vesicle-plasma membrane tether extension events in the presence and absence of GTPγS. A characteristic extension length consistent with unfolding of single α helices of the exocyst complex is observed, and GTPγS is shown to destabilize tethers, which is consistent with the importance of GTP-GDP cycling in tethering.

Finally, chapter 6 summarizes the present work and looks ahead to future directions.

REFERENCES

1. Burgoyne, R. D. & Morgan, A. Secretory granule exocytosis. *Physiol. Rev.* **83,** 581–632 (2003).

2. Burgess, T. L. & Kelly, R. B. Constitutive and regulated secretion of proteins. *Annu. Rev. Cell Biol.* **3,** 243–293 (1987).

3. James, D. J. & Martin, T. F. J. CAPS and Munc13: CATCHRs that SNARE Vesicles. *Front. Endocrinol. (Lausanne).* **4,** 187 (2013).

4. Pfeffer, S. R. Transport-vesicle targeting: tethers before SNAREs. *Nat. Cell Biol.* **1,** 17–22 (1999).

5. Söllner, T. *et al.* SNAP receptors implicated in vesicle targeting and fusion. *Nature* **362,** 318–324 (1993).

6. Weber, T. *et al.* SNAREpins: minimal machinery for membrane fusion. *Cell* **92,** 759–772 (1998).

7. Jahn, R. & Fasshauer, D. Molecular machines governing exocytosis of synaptic vesicles. *Nature* **490,** 201–207 (2012).

8. Munson, M. & Novick, P. The exocyst defrocked, a framework of rods revealed. *Nat. Struct. Mol. Biol.* **13,** 577–581 (2006).

9. Whyte, J. R. C. & Munro, S. Vesicle tethering complexes in membrane traffic. *J. Cell Sci.* **115,** 2627–2637 (2002).

10. Steyer, J. A. & Almers, W. Tracking single secretory granules in live chromaffin cells by evanescent-field fluorescence microscopy. *Biophys. J.* **76,** 2262–2271 (1999).

11. Johns, L. M., Levitan, E. S., Shelden, E. A., Holz, R. W. & Axelrod, D. Restriction of Secretory Granule Motion near the Plasma Membrane of Chromaffin Cells. *J. Cell Biol.* **153,** 177–190 (2001).

12. Pfeffer, S. Vesicle tethering factors united. *Mol. Cell* **8,** 729–730 (2001).

13. Cai, H., Reinisch, K. & Ferro-Novick, S. Coats, tethers, Rabs, and SNAREs work together to mediate the intracellular destination of a transport vesicle. *Dev. Cell* **12,** 671–682 (2007).

14. Li, F. *et al.* Energetics and dynamics of SNAREpin folding across lipid bilayers. *Nat. Struct. Mol. Biol.* **14,** 890–896 (2007).

15. Gao, Y. *et al.* Single reconstituted neuronal SNARE complexes zipper in three distinct stages. *Science* **337,** 1340–1343 (2012).

16. Fernández-Busnadiego, R. *et al.* Quantitative analysis of the native presynaptic cytomatrix by cryoelectron tomography. *J. Cell Biol.* **188,** 145–156 (2010).

17. Yu, I.-M. & Hughson, F. M. Tethering factors as organizers of intracellular vesicular traffic. *Annu. Rev. Cell Dev. Biol.* **26,** 137–156 (2010).

18. Hafez I Lindau M,, S. A. Compound exocytosis and cumulative fusion in eosinophils. *J. Biol. Chem.* **278,** 44921–44928 (2003).

19. TerBush, D. R., Maurice, T., Roth, D. & Novick, P. The Exocyst is a multiprotein complex required for exocytosis in Saccharomyces cerevisiae. *EMBO J.* **15,** 6483–6494 (1996).

20. Kee, Y. *et al.* Subunit structure of the mammalian exocyst complex. *Proc. Natl. Acad. Sci. U. S. A.* **94,** 14438–14443 (1997).

21. Grote, E., Carr, C. M. & Novick, P. J. Ordering the final events in yeast exocytosis. *J. Cell Biol.* **151,** 439–451 (2000).

22. Boyd, C., Hughes, T., Pypaert, M. & Novick, P. Vesicles carry most exocyst subunits to exocytic sites marked by the remaining two subunits, Sec3p and Exo70p. *J. Cell Biol.* **167,** 889–901 (2004).

23. Guo, W., Roth, D., Walch-Solimena, C. & Novick, P. The exocyst is an effector for Sec4p, targeting secretory vesicles to sites of exocytosis. *EMBO J.* **18,** 1071–1080 (1999).

24. Sato, Y., Fukai, S., Ishitani, R. & Nureki, O. Crystal structure of the Sec4p.Sec2p complex in the nucleotide exchanging intermediate state. *Proc. Natl. Acad. Sci. U. S. A.* **104,** 8305–8310 (2007).

25. Van Weering, J. R. T., Toonen, R. F. & Verhage, M. The role of Rab3a in secretory vesicle docking requires association/dissociation of guanidine phosphates and Munc18-1. *PLoS One* **2,** e616 (2007).

26. Novick, P. & Guo, W. Ras family therapy: Rab, Rho and Ral talk to the exocyst. *Trends Cell Biol.* **12,** 247–249 (2002).

27. Inoue, M., Chang, L., Hwang, J., Chiang, S.-H. & Saltiel, A. R. The exocyst complex is required for targeting of Glut4 to the plasma membrane by insulin. *Nature* **422,** 629–633 (2003).

28. Fernández-Busnadiego, R. *et al.* Cryo-electron tomography reveals a critical role of RIM1α in synaptic vesicle tethering. *J. Cell Biol.* **201,** 725–740 (2013).

29. Valero, V., Nevian, T., Ho, D. & Lindau, M. Tethering forces of secretory granules measured with optical tweezers. *Biophys. J.* **95,** 4972–4978 (2008).

CHAPTER 2

MEASUREMENT OF PROTEIN PROPERTIES BY APPLIED PULL FORCES

2.1 Introduction

Optical trapping, atomic force microscopy (AFM), and total internal reflection fluorescence (TIRF) microscopy combine to form a powerful set of tools for biophysical experiments. One application of optical trapping and AFM is in applying pull forces to proteins, which has provided much information about protein structure and dynamics. Such experiments have so far been performed on reconstituted or isolated proteins, requiring that the identity of the protein to be studied is already known. The following chapters will describe the development of pull force methods to directly study the mechanical properties of physiological tethers.

2.2 The Optical Trap

Optical trapping, first demonstrated in a single-beam gradient form by Arthur Ashkin in 1986[1], takes advantage of the phenomenon that a tightly focused laser beam will exert a trapping force on dielectric materials. The nature of this trapping force on a dielectric sphere can be readily understood in two regimes[2]. When the trapped sphere is much larger than the laser wavelength, the conditions for Mie scattering are satisfied, and ray optics may be used. The optical forces on the bead are then seen as arising from a transfer of momentum from the light to the sphere. Scattering and absorption result in a direct transfer of the light momentum to the sphere, and push the

sphere in the direction of laser propagation. The trapping force arises from refraction of photons (Fig. 2.1), which draw the sphere towards higher light intensity.

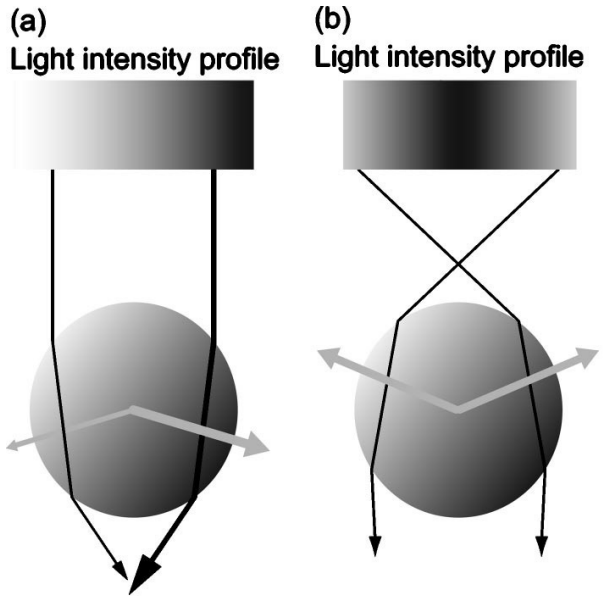

Figure 2.1. Force imparted to a dielectric sphere by a laser beam. The weights of the black arrows indicate intensity of the laser light, and the directions of the arrows indicate directions of propagation. The weights and directions of the gray arrows indicate the forces on the sphere that arise from conservation of momentum, and are equal and opposite the momentum changes imparted to the photons by refraction. Panel (a) demonstrates that the sphere will be attracted toward higher intensity light. Panel (b) demonstrates that a tightly focused laser beam gives rise to a trapping force toward the laser focus. Image from Neuman, K. C. & Block, S. M. Optical trapping. *Rev. Sci. Instrum.* **75,** 2787–2809 (2004).

When the trapped sphere is much smaller than the laser wavelength, the conditions for Rayleigh scattering are satisfied, and the sphere can be treated as a point dipole[2]. In this case, absorption and emission of photons by the sphere push the sphere in the direction of laser propagation, due to the random direction of motion of the emitted photons. The trapping force arises because the laser light induces a dipole in the sphere, which is then pushed in the direction of the intensity gradient.

For force measurements, the strength of the force on a trapped object, such as a vesicle, must be calibrated. This can be done using the viscous drag method[3]. The sample chamber is moved relative to the trap at known speed (Fig. 2.2). The viscous drag of the surrounding fluid displaces the trapped object from the trap center such that the restoring force of the trap balances the applied viscous drag force. The viscous drag force is calculated using the assumption of Stokes flow conditions. A first order correction for surface interactions is applied[4], giving

$$\vec{F}_{viscosity} = \frac{3\pi d\eta\vec{v}}{1-(9/32)(d/h)}, \tag{2.1}$$

where $\vec{F}_{viscosity}$ is the force on the vesicle from the moving buffer, d is the vesicle diameter, η is the buffer viscosity at the ambient temperature, $\vec{v}$ is the velocity of the dish holding the sample, and h is the height of the vesicle above the surface. The trapping potential experienced by the vesicle can be approximated as harmonic[3],

$$\vec{F}_{trap} = -k\vec{x}, \tag{2.2}$$

where $\vec{F}_{trap}$ is the force exerted by the trap on the vesicle, k is a constant describing the strength of the trapping potential, and $\vec{x}$ is the displacement of the vesicle from the center of the trap potential. Thus, the strength of the vesicle-trap interaction is given by:

$$k = \frac{3\pi d\eta v}{x(1-(9/32)(d/h))}. \tag{2.3}$$

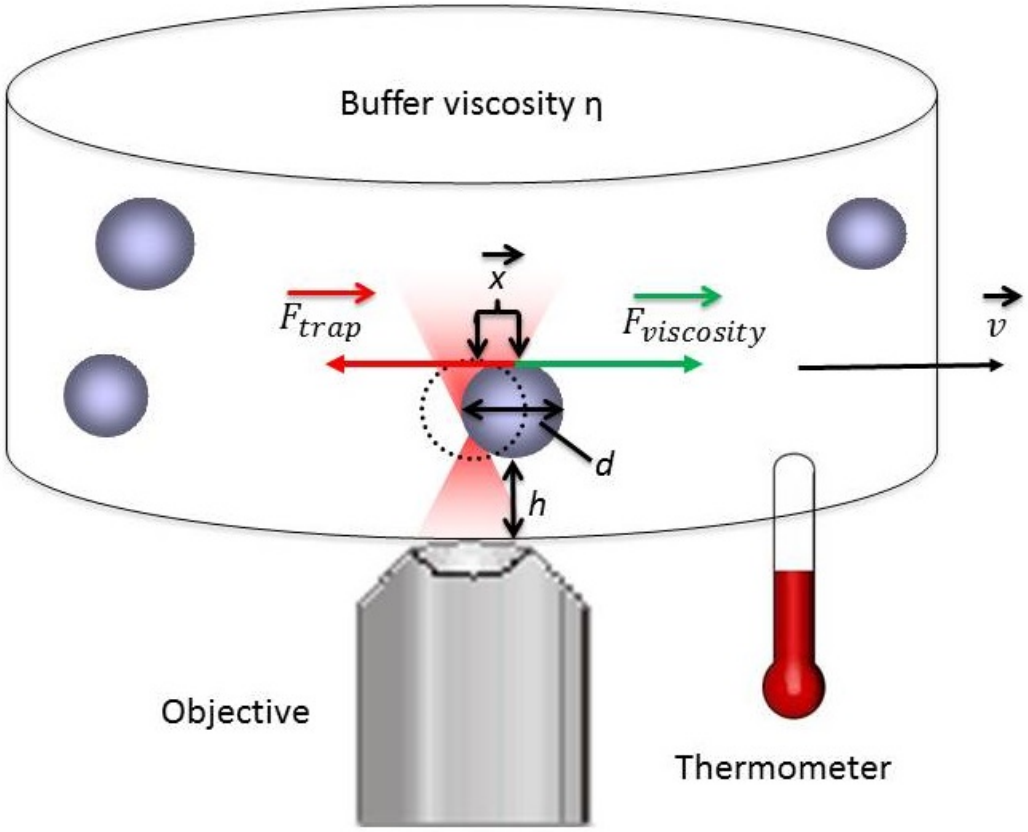

Figure 2.2. The viscous drag calibration method. The sample dish is moved at known velocity relative to the objective, which exerts a known viscous drag force. The vesicle displacement from the trap center then reveals the trap stiffness.

2.3 The Atomic Force Microscope

The atomic force microscope (AFM) was first demonstrated in 1986 as a means to measure surface topography at Å resolution[5]. The AFM measures the force of interaction between a small, flexible cantilever and a sample surface. The cantilever height above the surface is precisely controlled with a piezoelectric servo. The cantilever carries a probe with a sharpened tip. The cantilever deflects as the tip interacts with the sample surface (Fig. 2.3). A laser is reflected off of the cantilever and onto a quad photodiode (QPD), generating a voltage signal called the "cantilever

deflection signal," V_{defl}. As the cantilever deflects, the position of the laser on the QPD shifts, resulting in a change to V_{defl}. The V_{defl} signal is sufficient to determine the cantilever deflection, which may be used to measure surface topography with a cantilever in contact with the surface (Fig. 2.3A,B). In practice, the cantilever height may be adjusted to maintain constant deflection, and the cantilever height then maps topographical features on the sample surface.

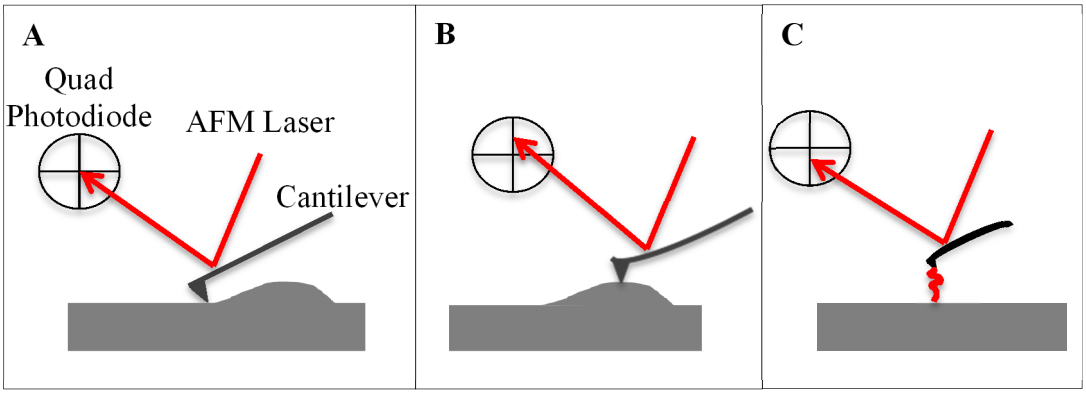

Fig 2.3. Surface topography and pull force measurement by atomic force microscopy. Panel A shows a cantilever in contact with a sample surface, with a laser reflected onto a quad photodiode. In panel B, the tip is deflected by a feature on the surface, changing the angle at which the laser is reflected, and therefore the quad photodiode signal. In panel C, the cantilever is pulling on a sample, resulting in deflection in the opposite direction to the deflection in panel B.

If the cantilever stiffness is known, the magnitude of the force acting on the cantilever can be determined. This opens up the possibility of applying known pull forces to a sample[6] (Fig 2.3C). First, the sensitivity of the V_{defl} signal to deflection of the cantilever, referred to as the "deflection sensitivity," must be measured. This is done by pressing the cantilever tip into a hard surface by a controlled distance. The resulting change in V_{defl} is measured, providing the deflection sensitivity. The deflection sensitivity will depend not only on the cantilever in use, but also on the precise alignment of the AFM laser.

A well-established method of cantilever stiffness calibration is the "Thermal K" method[7], which uses the equipartition of energy in thermal fluctuations of the cantilever. For small cantilever deflections, the cantilever is treated as a harmonic oscillator. The equipartition theorem then states that the potential energy

$$< (1/2)kz^2 >= (1/2)k_B T\,, \tag{2.4}$$

where m is the effective mass of the oscillator, k is the Hookian spring constant of the oscillator, z is the cantilever tip displacement, k_B is the Boltzmann constant, and T is temperature. In principle, k can then be determined by calculating $<x^2>$. However, noise sources other than thermal excitation contribute to $<x^2>$. This problem can be addressed by measuring the power spectral density of the oscillations and integrating a Lorentzian fit to the peak that is due to thermal excitation. This integral is equal to the mean square fluctuations resulting from thermal fluctuations[7]. Multiple refinements of this method have been developed to account for complications that cause deviation from the model of a simple harmonic oscillator, such as higher order modes of oscillation of the cantilever[8] and the tilt of the cantilever[9].

2.4 The Total Internal Reflection Fluorescence Microscope

Total Internal Reflection Fluorescence (TIRF) microscopy has been used to monitor secretory vesicle motion near the cell membrane, detecting vertical position changes as small as 4 nm[10,11]. TIRF makes use of the evanescent wave that penetrates a boundary when incident light is reflected from it at or above the critical angle. According to Snell's Law, when light passes from medium 1 to medium 2:

$$n_1 \sin\theta_1 = n_2 \sin\theta_2 , \tag{2.5}$$

where n_1 is the refractive index of medium 1, n_2 is the refractive index of medium 2, θ_1 is the angle between the incident light and the normal to the interface, and θ_2 is the angle between the refracted light and the normal to the interface. The critical angle, θ_c, is defined by

$$\sin\theta_c = n_2 / n_1 . \tag{2.6}$$

When $\theta_1 = \theta_c$, then $\theta_2 = 90^o$. However, when the light is incident at or above the critical angle, an evanescent wave penetrates still into medium 2, as required to satisfy the boundary conditions of the electric field at the interface. The intensity of the evanescent wave decays rapidly according to the equation:

$$I(z) = I_0 \exp(-z / d), \tag{2.7}$$

where I is the evanescent wave intensity, I_0 is the evanescent wave intensity at $z = 0$, z is the distance from the interface into medium 2, and d is called the penetration depth, which is given by:

$$d = \lambda / [4\pi (n_1^2 \sin^2\theta_1 - n_2^2)^{1/2}], \tag{2.8}$$

where λ is the wavelength of the incident light[12].

The rapidly decaying evanescent wave can be very useful as a source of fluorescence excitation. When a laser is reflected off the bottom of a sample at or above θ_c, the resulting monochromatic evanescent wave will provide illumination only within 100 nm or so of the bottom surface of the sample. Additionally, because of the rapid and well-defined decay rate of the evanescent wave intensity, changes in vertical position of fluorescing objects can be detected as changes in fluorescence intensity.

2.5 Studies of Biological Molecules under Applied Force

AFM and optical trap pulling experiments have provided much information about protein structure and dynamics. The muscle protein titin has been a subject of much study using the AFM pulling methods[13]. In force-extension experiments, an AFM tip attaches to a protein and pulls on it, resulting in a sawtooth pattern in the force vs extension trace as the domains of the titin protein unfold one-by-one (Fig. 2.4). If a single protein is attached, the peaks in the sawtooth will be evenly spaced. The worm-like chain model[14] predicts the relationship between the extension of the molecule and the pull force applied to it. This model can be fit to a single peak in the sawtooth pattern, corresponding to unfolding of a single domain, to determine the increase in the contour length of the protein resulting from unfolding of a domain[13]. This procedure provides a "fingerprint" unique to the molecule.

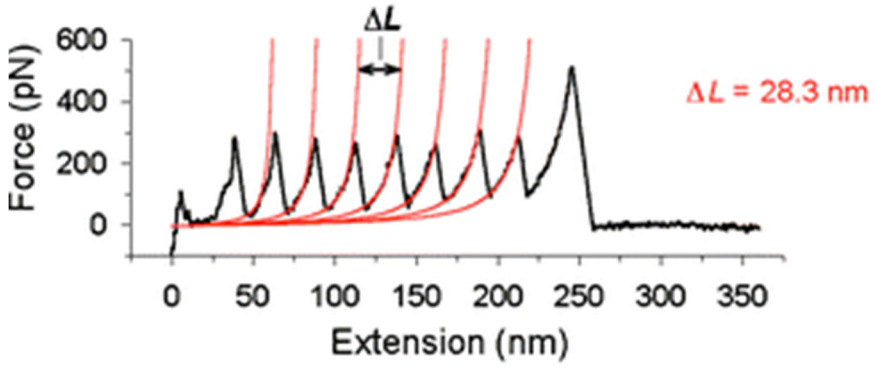

Figure 2.4. Force-extension pulling on a titin molecule. The force vs extension curve (black trace) shows a sawtooth pattern, with each peak corresponding to unfolding of a single domain. The red lines are fits of the worm-like chain model to each peak. ΔL is the change in contour length corresponding to unfolding of each domain. Image adapted from Linke, W. A. & Grützner, A. Pulling single molecules of

titin by AFM - recent advances and physiological implications. *Pflugers Arch.* **456,** 101–115 (2008).

Force-clamp, an alternate method to the force-extension approach, applies a constant pull force to the molecule, resulting in stair-step patterns in which each step corresponds to the unfolding of a single domain, and more mechanically stable proteins take longer to unfold[15]. Additionally, force-clamp experiments on reconstituted SNARE proteins using optical traps successfully stabilized a half-zippered state of the SNARE complex and measured the extension change related to zippering of different domains using the worm-like chain model[16].

2.6 Conclusions

The methods described here are a powerful set of tools that have found use in a range of biophysical experiments. Specifically, AFM and optical trap pulling experiments have proven useful in studying the mechanical properties of proteins and protein unfolding. However, such experiments have been primarily performed on reconstituted or isolated molecules, in which the identity of the molecule to be was already known. In the following chapters, we develop methods of performing force-clamp experiments directly on vesicle-vesicle and vesicle-plasma membrane tethers, allowing the study of the mechanical properties of the tether prior to identification of the proteins that constitute the tether, and possibly allowing identification of these proteins.

REFERENCES

1. Ashkin, A., Dziedzic, J. M., Bjorkholm, J. E. & Chu, S. Observation of a single-beam gradient force optical trap for dielectric particles. *Opt. Lett.* **11,** 288–290 (1986).

2. Neuman, K. C. & Block, S. M. Optical trapping. *Rev. Sci. Instrum.* **75,** 2787–2809 (2004).

3. Felgner, H., Müller, O. & Schliwa, M. Calibration of light forces in optical tweezers. *Appl. Opt.* **34,** 977–982 (1995).

4. Svoboda, K. & Block, S. M. Biological applications of optical forces. *Annu. Rev. Biophys. Biomol. Struct.* **23,** 247–285 (1994).

5. Binnig, G. & Quate, C. F. Atomic force microscope. *Phys. Rev. Lett.* **56,** 930–933 (1986).

6. Heinz, W. F. & Hoh, J. H. Spatially resolved force spectroscopy of biological surfaces using the atomic force microscope. *Trends Biotechnol.* **17,** 143–150 (1999).

7. Hutter, J. L. & Bechhoefer, J. Calibration of atomic-force microscope tips. *Rev. Sci. Instrum.* **64,** 1868–1873 (1993).

8. Butt, H.-J. & Jaschke, M. Calculation of thermal noise in atomic force microscopy. *Nanotechnology* **6,** 1–7 (1995).

9. Hutter, J. L. Comment on tilt of atomic force microscope cantilevers: effect on spring constant and adhesion measurements. *Langmuir* **21,** 2630–2632 (2005).

10. Allersma, M. W., Bittner, M. A., Axelrod, D. & Holz, R. W. Motion matters: secretory granule motion adjacent to the plasma membrane and exocytosis. *Mol. Biol. Cell* **17,** 2424–2438 (2006).

11. Toonen, R. F. *et al.* Dissecting docking and tethering of secretory vesicles at the target membrane. *EMBO J.* **25,** 3725–3737 (2006).

12. Kisler Elliott, K. J. Electrochemical detection and total internal reflection fluorescence microscopy: illuminating the exocytotic mechanism. (2009).

13. Linke, W. A. & Grützner, A. Pulling single molecules of titin by AFM - recent advances and physiological implications. *Pflugers Arch.* **456,** 101–115 (2008).

14. Marko, J. F. & Siggia, E. D. Stretching DNA. **28,** 8759–8770 (1995).

15. Bujalowski, P. J. & Oberhauser, A. F. Tracking unfolding and refolding reactions of single proteins using atomic force microscopy methods. *Methods* **60,** 151–160 (2013).

16. Gao, Y. *et al.* Single reconstituted neuronal SNARE complexes zipper in three distinct stages. *Science* **337,** 1340–1343 (2012).

CHAPTER 3

A METHOD TO DISTINGUISH VESICLE-VESICLE TETHERING AND FUSION IN A DUAL OPTICAL TRAP USING FLUORESCENT DYE TRANSFER

3.1 Abstract

Although several proteins have been implicated in secretory vesicle tethering, the identity and mechanical properties of the components that form the physical membrane link remain unknown. Isolated eosinophil vesicles perform homotypic fusion, and have been observed to bind very tightly to each other in vitro, such that they could in some cases not be dissociated by an optical trap. We present a method to determine whether these tightly bound vesicles are tethered or fused using simultaneous optical trapping and fluorescence microscopy. The vesicles were loaded with a fluorescent marker, brought into contact, and allowed to bind. Vesicles that bound to each other dissociated in an all-or none fashion at pull forces < 30 pN. The approach is potentially suitable to distinguish tethered and fused states.

3.2 Introduction

The fusion of secretory vesicles occurs from a tethered state, in which the vesicles are associated with the target membrane via long-range interactions that do not require the cytoskeleton[1]. Tethering interactions have also been observed between secretory vesicles that undergo homotypic fusion in compound exocytosis [2,3]. The identities and mechanical properties of the proteins that form the physical tether are not known[4].

Multiple protein complexes have been implicated in exocytosis. Among them are long coiled-coil proteins and multi-subunit tethering complexes (MTCs)[1]. Many MTCs contain CATCHR (Complex Associated with Tethering Containing Helical Rods) domains, characterized by an extended rod-like structure composed of helical bundles[1,5]. These CATCHR domains promote an elongated structure and mediate interactions with other proteins, such as GTPases. Among the CATCHR proteins that have been implicated in vesicle tethering are the exocyst complex, Conserved Oligomeric Golgi (COG) complex, Dsl1 complex, Golgi-associated Retrograde Protein (GARP) complex, Calcium-dependent Activator Protein for Secretion (CAPS), Munc13, and the class V myosin Myo2. The HOPS (Homotypic Fusion and Vacuole Protein Sorting) complex, which likely provides the tethering required for homotypic fusion between large organelles, such as in compound exocytosis of eosinophilic granules, lacks CATCHR domains.

Optical trap pulling experiments on isolated horse eosinophil vesicle-vesicle tethers[2] revealed three distinct tethered states. Additionally, some vesicle pairs bound so tightly that they could not be dissociated using the optical trap, raising the question of whether the tightly-bound vesicles were fused, rather than tethered. Horse eosinophil granules do not change shape during vesicle-vesicle fusion[3], so another means of detecting fusion is required. In the present work, optical trap pulling experiments were performed where vesicles were differentially loaded with a fluorescent marker. If the vesicles fused to each other on contact, the fluorescent marker should transfer and equalize between them[3], identifying whether the vesicle-vesicle pair is in a strongly tethered state or already fused.

3.3 Methods

3.3.1 Trapping and Fluorescence Imaging Apparatus

Fig. 3.1 is a diagram of the fluorescence and trapping optics. The trapping laser was a YLR-20-1064-LP from IPG Photonics (Oxford, MA), operated at 8W. The laser was first directed through a half wave plate and polarizing beam splitter (PBS), allowing a controlled amount of beam power to be directed into a beam dump as necessary to control the intensity of the final trapping beam. A second wave plate and PBS pair split the laser into two separate beams. One beam passed through a DTD-274HA6 2-axis acousto optic deflector (AoD) (IntraAction, Bellwood, IL) to enable steering of the beam. Both beams were then directed into the rear port of an Axiovert 135TV microscope (Zeiss, Oberkochen, Germany) such that they overfilled the back aperture of a FLUAR 100x, 1.3NA objective (440285, Zeiss, Oberkochen, Germany), which focused the beams into traps at the objective focus. A pair of lenses in the path of the movable beam corrected for the path length difference of the two beams, so they would have the same width and divergence upon reaching the objective back aperture. The lenses also served to establish the AoD and the objective back aperture as conjugate planes, so that a beam rotation at the AoD resulted in translation of the beam as it exited the objective. In this way, two separate traps were formed, one of which was steered by adjusting the AoD driving frequency.

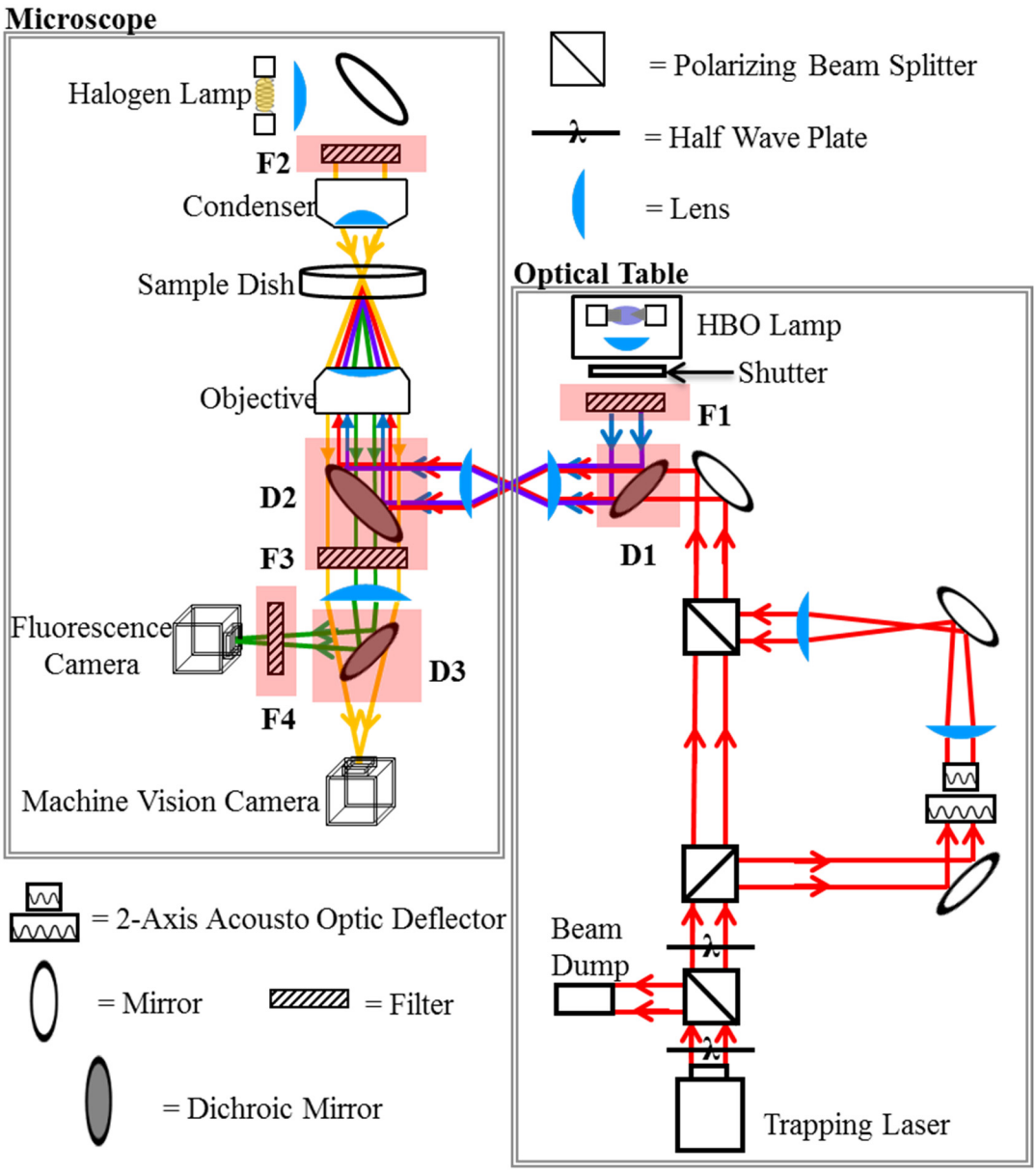

F1 = Excitation Filter, Transmits 460 nm to 500 nm
F2 = Long Pass Filter, Transmits above 570 nm
F3 = Band Pass Filter, Transmits 500 nm to 750 nm
F4 = Emission Filter, Transmits 500 nm 550 nm
D1 = Transmits > 530 nm, Transmits 1064 nm
D2 = Transmits > 500 nm, Reflects 1064 nm
D3 = Transmits > 550 nm, Transmits 1064 nm
= Trapping Laser, 1064 nm
= Fluorescence Excitation, 460 nm to 500 nm
= Bright Field Light, > 570 nm
= Fluorescence Emission, 500 to 550 nm

Figure 3.1 Diagram of the optics for the trap and fluorescence. Components shaded in pink boxes were added to enable fluorescence imaging.

For experiments, the samples were contained in dishes on the microscope stage at the objective focus. The dishes were 10 x 35 mm dishes with 5 mm high sides, into the center of which 10 mm round holes were precision cut. Round 18 mm #1 coverslips (catalog no. 12-545-84, Fisherdbrand, Pittsburgh, PA) were attached to the bottoms of the dishes under the holes in the center using an RTV615 Silicone Potting Compound kit. Samples were placed in the centers of the dishes on the coverslip surface, and the dish allowed for simple mounting on the microscope stage.

An HBO 103 W/2 (Osram, Munich, Germany) was used as a light source for fluorescence excitation. The fluorescent label used was LysoTracker Green DND-26 (Invitrogen, Carlsbad, CA), which has excitation/emission maxima at ~504/511 nm. LysoTracker probes include a base that is only partially protonated at neutral pH. The probes accumulate and are retained in acidic compartments, such as the eosinophil vesicles used in these experiments, due to protonation resulting from the lower pH environment [6].

Fig. 3.1 shows how optical filters and dichroic mirrors were used to enable simultaneous optical trapping, fluorescence imaging, and bright field imaging. All optical filters and dichroic mirrors used were ordered from Chroma, Bellows Falls, VT. First, the light from the HBO passed through a HQ480/40x excitation filter (F1). The light that passed through F1 (fluorescence excitation) was introduced into the laser beam path using a 530dcxr-xt dichroic mirror (D1), which reflected the fluorescence excitation while transmitting the trapping laser. The fluorescence

excitation and laser beam then entered the microscope and reflected off of a uv/500/nir-pc dichroic mirror (D2), into the objective back aperture, where they provided excitation of Lysotracker Green and vesicle trapping, respectively.

The light source for bright field imaging was the microscope's halogen lamp, which emitted bright field light that passed through a HQ570LP filter (F2), leaving only wavelengths greater than 570 nm. The bright field light then passed through the microscope condenser and illuminated the sample.

The bright field light and the light emitted by LysoTracker Green (fluorescence emission) exited the sample dish and entered the objective. The light was directed back through D2 again, as well as a HQ625/250M-2P band pass filter (F3), which removed any of the fluorescence excitation and trapping laser that were backscattered from the sample. A 550dcxr dichroic mirror (D3) split the bright field light and fluorescence emission, sending the fluorescence emission to a CCD camera for fluorescence imaging (Quantix from Photometrics, Tucson, AZ), and the bright field light to a CMOS camera for vesicle imaging and machine vision (CV640 from Allied Vision Technologies, formerly Prosilica, Newburyport, MA). A HQ525/50M-2P emission filter (F4) immediately in front of the fluorescence camera blocked any remaining bright field light.

3.3.2 Trap Control Apparatus

Fig. 3.2 shows a block diagram of the equipment that controlled the trap and fluorescence imaging. The fluorescence camera interfaced with a computer running V++ software (Digital Optics, Auckland, New Zealand), while the machine vision

camera interfaced with a computer running a custom-written trap control program in LabVIEW 7.1.1 with NI Vision. The "exposing" output of the fluorescence camera was connected to a DAQ PCI-MIO-16XE-50 (National Instruments, Austin, TX), which in turn was connected to the computer running the trap control program. This allowed synchronization of the fluorescence images with the data recorded by the trap control program.

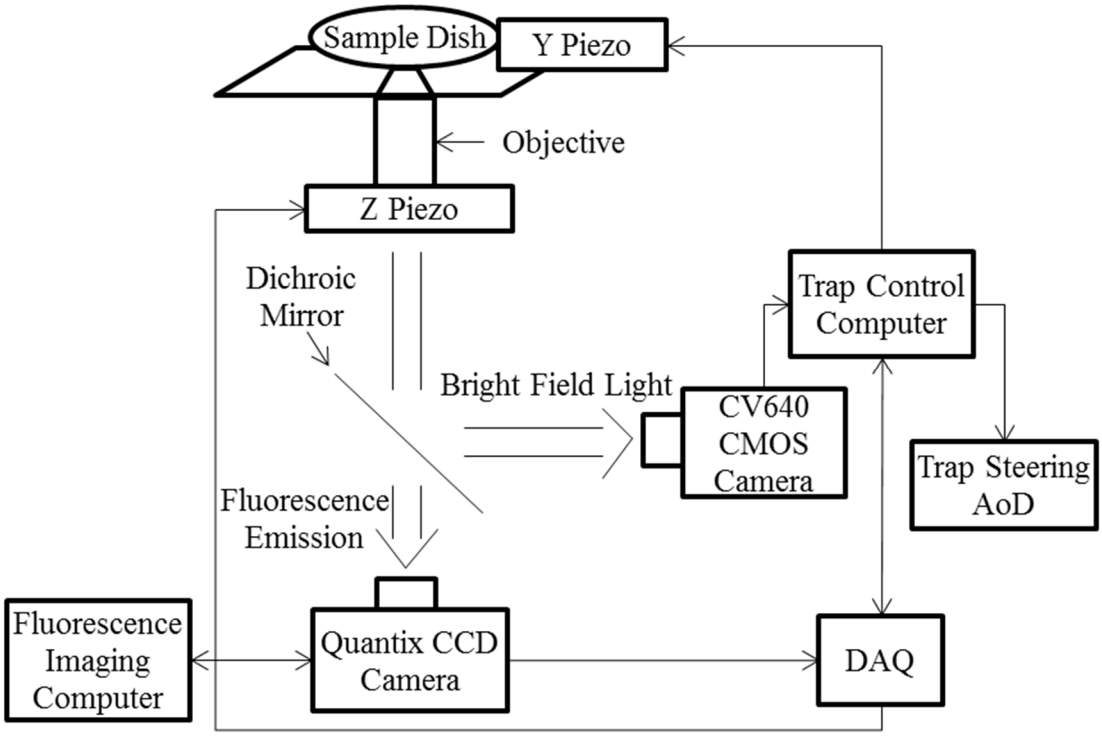

Figure 3.2 Diagram of trap and fluorescence control equipment.

The objective was mounted on a piezo, here called the z piezo (P-721.10 with E-662.LR controller, Physik Instrumente, Karlsruhe/Palmbach, Germany), that allowed for precise control of objective z position. The sample was mounted on a separate piezo, the y piezo (P-783.ZL with E-662.LRX controller, Physik Instrumente, Karlsruhe/Palmbach, Germany), which allowed for horizontal movement relative to the objective, necessary for the viscous drag calibration method to be described in

section 3.3.6. The y piezo had nonlinearity not exceeding a magnitude of 0.1%, or 0.3 microns, in the range from 0 to 100 microns. A joystick provided control of the microscope stage in both the x and y directions. Floating vesicles were captured in the traps by moving the stage with the joystick. Once vesicles were trapped, the trap control program controlled the position of the movable trap by altering the frequencies of the trap steering AoD.

3.3.3 Isolation of Horse Eosinophil Granules

Eosinophils were isolated from horse blood, according to the method of Valero et. al[2], and stored in 10 mL of Medium 199 (12350, Gibco, Life Technologies, Carlsbad, CA). Before experiments, 250 µL each of the medium with cells was transferred to two centrifuge tubes, and 1 µL of Lysotracker Green was added to one of the tubes. The cells were allowed to incubate in the dye for 10 minutes, and then both centrifuge tubes were spun down in a Heraeus Instruments Megafuge 1.0R (Thermo Fisher Scientific Inc., Waltham, MA) at 300 g for 5 minutes to pellet the cells.

A KCl buffer (vesicle isolation buffer) developed by Valero et. al. [2] was used for experiments with isolated eosinophil vesicles. The vesicle isolation buffer contained: 125 mM KCl, 10.3 mM NaCl, 10 mM HEPES, 7.02 mM $MgCl_2$, 2 mM $CaCl_2$, 3.3 µ/mL Pepstatin A (P-4265, Sigma-Aldrich, St. Louis, MO), 1.6 µg/mL TPCK (T-4376, Sigma-Aldrich, St. Louis, MO), 13.2 µg/mL Aprotinin (A-3428, Sigma-Aldrich, St. Louis, MO), 1.67 µg/mL Leupeptin (L-2884, Sigma-Aldrich, St. Louis, MO), 5 µg/mL DNase I, grade II (10104159001, Roche Diagnostics,

Indianapolis, IN), and 3.3 mM DTT (15508-013, Invitrogen, Carlsbad, CA). pH was 7.16 – 7.18, measured with an Orion Star A111 pH meter from Thermo Fisher Scientific Inc. (Waltham, MA). Osmolality was 326 – 339 mmol/kg, measured with a VAPRO 5520 Vapor Pressure Osmometer from Wescor, Inc. (Logan, UT). The DNase, DTT, and protease inhibitors were added to the buffer on the day of the experiments. The stock solutions for these same-day ingredients included some chemicals that were then present in the final buffer. The final concentrations of these chemicals were: 3.38 μL/mg 200 proof ethanol, 2.5 μL/mL glycerol, and 0.05 mM tris.

To transfer the cells from Medium 199 to the vesicle isolation buffer, a pipette was used to remove as much of the medium from the cell pellet as possible, and 100 μL buffer was added, on top of the cell pellet. The buffer was then again removed by pipette, and 100 μL fresh buffer was added. The cells in each tube were then lysed by ~ 50 passes through a 25G 1.5 inch needle. The exact number of passes depended on the particular sample and its age. Separate needles and syringes were used for samples with Lysotracker Green and without. Using a pipette, 10 – 25 μL of the resulting suspension was taken from each tube and added to the sample dish. 100 μL of buffer was added to dilute the sample.

3.3.4 Vesicle Tracking by Machine Vision

The bright field images were used to measure vesicle displacements. The trap control program extracted images from the camera at a frame rate of 50 fps. An ROI was drawn by hand around all or part of the vesicle that was to be tracked. The ROI

was extracted and saved as a template image. During image acquisition, the built-in NI Vision template-matching algorithm "Match Pattern" searched each frame for the template, and reported its position. The design of the experiment required that two vesicles be present in the field of view. To avoid confusion between the vesicles, the template matching search region was limited to a small area around the vesicle of interest. Each time the vesicle moved, the search region was moved with it. In this way, the search region always included most of the vesicle of interest and excluded the other vesicle.

3.3.5 Calibration of Pixel Size in Bright Field Imaging

To ensure high precision vesicle size and position measurements, the actual pixel size was measured (Fig. 3.3). A piece of material attached to a glass coverslip was tracked with the template matching algorithm described in section 3.3.4. The y

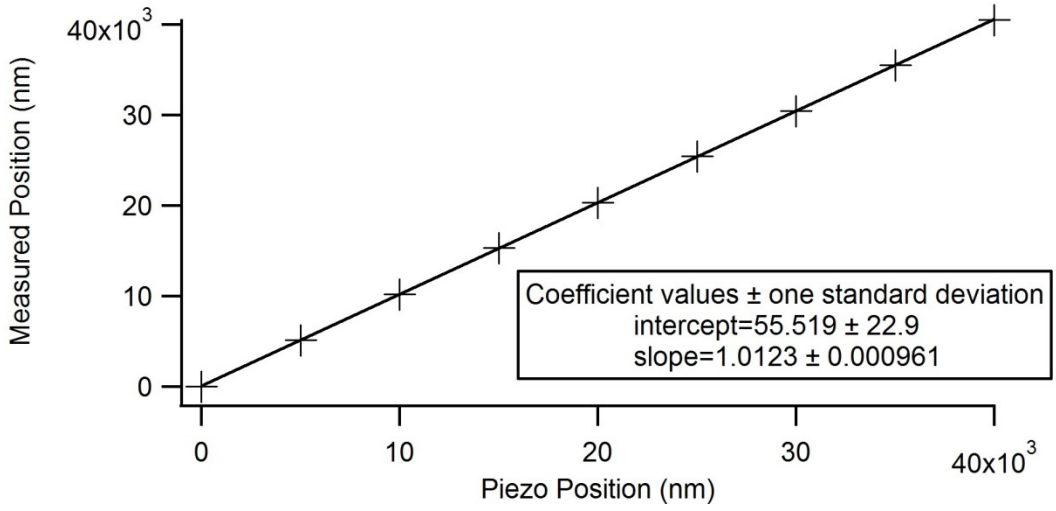

Figure 3.3. Trap pixel size calibration. Measured displacement is calculated using a pixel size of 95.33 nm. The linear fit shows good agreement with positions set using the y piezo.

piezo was moved in regular, 5 μm intervals over a 40 μm range. By plotting the real displacement vs the displacement reported by template matching, the pixel size was found to be 95.33 nm.

3.3.6 Trap Stiffness Calibration by the Viscous Drag Method

Determination of forces between two trapped vesicles required that the strength of the trapping interaction (trap stiffness) be known for one of the trapped vesicles. This was determined by the viscous drag method[7]. The vesicle was held in the trap while the y piezo was moved at a known speed. The viscous drag of the surrounding fluid displaced the vesicle from the trap center such that the restoring force of the trap balanced the applied viscous drag force. The trap stiffness was calculated as described in section 2.2:

$$k = \frac{3\pi d\eta v}{x(1-(9/32)(d/h))}, \tag{3.1}$$

where k is the trap stiffness, d is the vesicle diameter, η is the buffer viscosity at the ambient temperature, v is the velocity of the dish holding the sample, x is the displacement of the vesicle from the center of the trap, and h is the height of the vesicle above the surface

For each vesicle pair, one of the k values was measured before any contact between the two vesicles. LabVIEW was programmed to execute a quick analysis of the viscous drag data, so that k values could be obtained quickly and used in a force feedback loop. The viscous drag force was exerted by moving the sample dish back and forth at a single fixed speed. This meant that the vesicle was either at rest in the

center of the trap (beginning and end of the recording) or displaced in the positive or negative direction. A histogram of all recorded positions was generated, and a Gaussian was fit to each peak (Fig. 3.4). The distances between the peaks provided the values of *x* for Eq. 3.1.

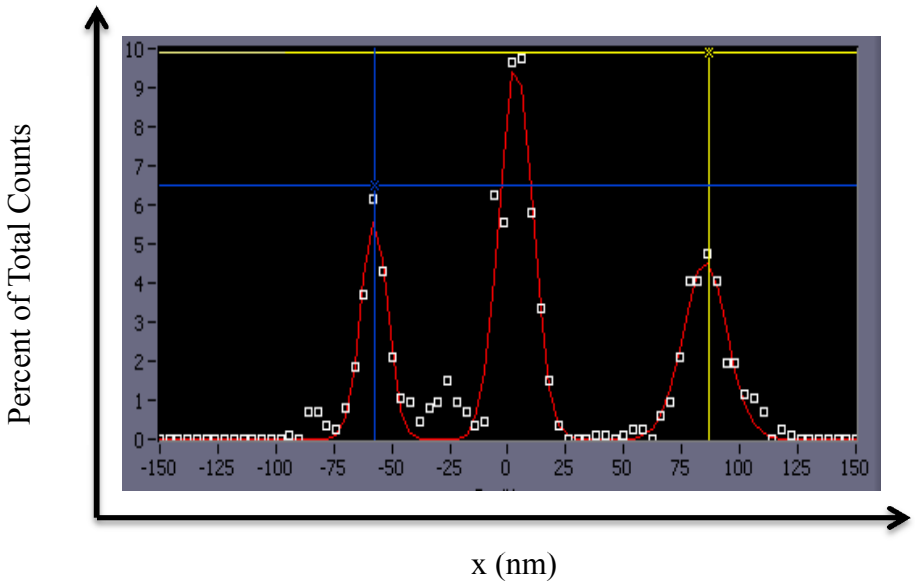

Figure 3.4. Histogram of vesicle positions recorded during a calibration, with Gaussian fits to each peak. In this case, the velocity of the sample dish during the calibration was 200 µm/s. The *x* values were 46 nm and 62 nm. The value used to calculate trap stiffness was 46 nm, because the vesicle was pulled towards negative *x* values when the pull force was applied.

To complete calculation of *k*, trapping depth also needed to be known. Trapping depth was estimated as 5µm, and each vesicle was adjusted to approximately that height before calibration. This had to be done without allowing a trapped vesicle to touch the coverslip surface, which would cause the vesicle to irretrievably stick to the coverslip. Passivating agents were not used to ensure that they would not interfere in measurements of the vesicle-vesicle interactions. Therefore, before experiments, a vesicle was found that was firmly attached to the surface, and a series of images of

that vesicle was taken at increasing heights above the surface (Fig. 3.5). The image series reveals that the dark center of the vesicle image vanishes at a height of approximately 5 μm. When a trapped vesicle was to be calibrated, a nearby vesicle attached to the coverslip surface was observed, and the focus was adjusted until the dark center of the attached vesicle just began to vanish.

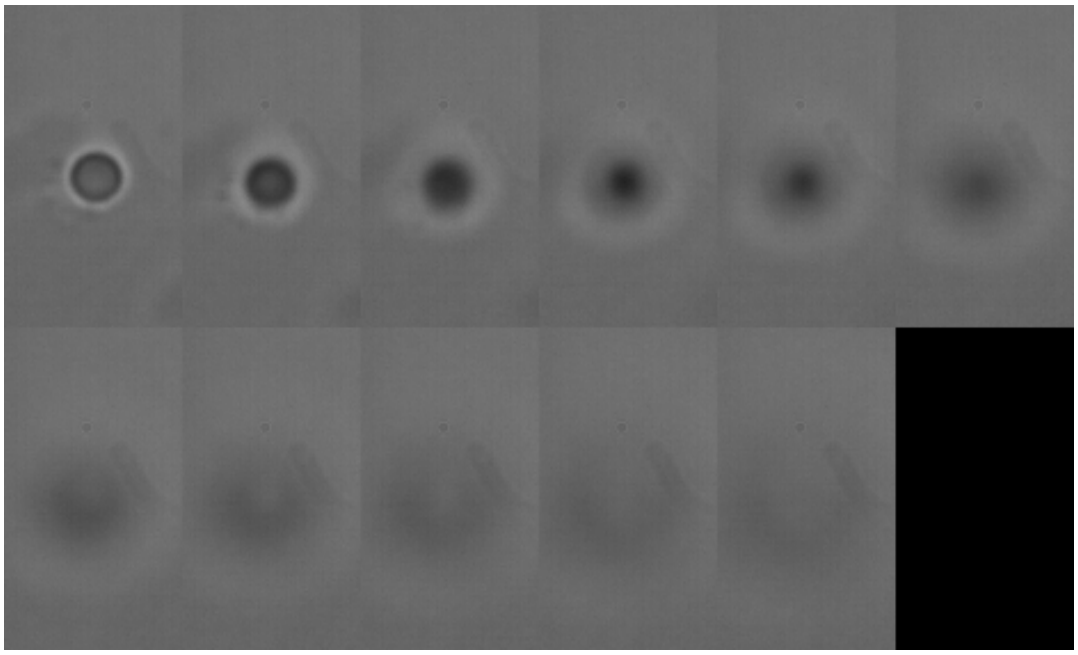

Figure 3.5. Appearance of a vesicle stuck to the surface as the objective is moved out of focus. In the upper left frame, the vesicle is in focus. In each successive frame, the objective height is increased 1μm.

The final piece of information needed to determine *k* was vesicle diameter. This was found by plotting the intensity profile along a line through the vesicle center and identifying the minima, which corresponded to the vesicle edges. Vesicle diameters ranged from 1.5 to 2.3 μm, and stiffnesses ranged from 0.015 to 0.083 pN/nm.

3.3.7 Dye Transfer Experiments

Once a vesicle was held in each trap, and the *k* value for the fixed trap vesicle was determined, the LabVIEW program brought the movable vesicle toward the fixed vesicle by adjusting the AOD frequency. The vesicles moved toward each other until they reached a push force, as indicated by the vesicle in the fixed trap being displaced from its trap center. To prevent noise from triggering false contact, a threshold in the slope of the force on the vesicle with time had to be exceeded over several data points. The threshold slope and number of data points used were determined by trial and error as 0.5 pN/s slope and 50 points (1 s). These values reliably indicated contact without pushing the vesicles together hard enough to force them from their traps. A push force was then maintained for 5 s to allow the vesicles to bond, and the movable trap was retracted to maintain a fixed pull force for 20 s. After 20 s, the pull force was increased. This process continued for 4 steps, or until the vesicle dissociated or one of the vesicles was pulled out of its trap.

During the experiment, the fluorescence camera recorded the Lysotracker Green emission. The LabVIEW program recorded the camera "exposing" output so the fluorescence recording could be synchronized with the other data.

3.3.8 Tracking Vesicle Intensity Changes in Dye Transfer Experiments

To determine whether any dye transfer between vesicles occurred, the fluorescence emission intensity of each vesicle, relative to initial fluorescence emission intensity, was determined in each frame of the fluorescence recordings. Since the vesicles were moving during the experiment, a template-matching procedure

custom-written in Igor Pro was used to track vesicle positions and intensities. The image of each vesicle in the first frame was taken as a template, and the procedure searched for that image in the nearby region in the next frame. As the vesicle moved, the region searched moved with it, in the same way as the template matching-algorithm in the trap control program did during the experiments. This avoided confusion between the two vesicles.

To measure the change in the vesicle intensity, the template-matching algorithm also included a multiplication factor (Scale) and offset (Background) in the fit of the intensity profile to the template image. The Scale factor indicated the vesicle intensity relative to initial intensity. The Background factor allowed a spatially constant background illumination to be subtracted from each frame of the recording.

3.3.9 Calculation of Vesicle Intensity per Volume

To determine whether vesicle-vesicle fusion took place, the total fluorescence intensity per volume, or intensity concentration (C_I) of each vesicle was determined. C_I is expected to be proportional to the Lysotracker Green concentration in the vesicle, and if two vesicles in contact fused, then the Lysotracker Green concentration, and therefore C_I, would equalize.

To find C_I, a value for the total intensity of a vesicle was needed. In the first frame of each fluorescence recording, the Igor "Image Line Profiles" tool was used to measure the intensity profile of a 3 pixel-wide bar across the center of each vesicle. A Gaussian fit with y offset was performed to the profile, and the y offset value was subtracted from the profile. Igor's area() function, which uses trapezoidal integration,

was used to find the area under both the measured intensity profile and the Gaussian fit to the profile, and the ratio of fit area to profile area was calculated. Among all vesicles, the ratio that was most different from 1 was 0.956, with the mean ratio being 0.995 and the standard deviation of ratios being 0.007, indicating that the vesicle intensity profiles were well approximated by the Gaussian. Therefore, the volumes of 2D Gaussian fits to the vesicle intensity distributions provided the total intensity values for the vesicles. Igor was used to perform a 2D Gaussian fit of the form

$$z_0 + A\exp[\frac{-1}{2}((\frac{x-x_0}{\sigma_x})^2 + (\frac{y-y_0}{\sigma_y})^2)] \tag{3.2}$$

to each vesicle. The volume under the fit was then:

$$I_{total} = 2\pi A\sigma_x\sigma_y\,. \tag{3.3}$$

Igor's "Image Line Profiles" tool was used to measure the intensity profile of the bright field image of the vesicle, providing the vesicle diameter, $d_{vesicle}$, as in section 3.3.6. The dye concentration in fluorescence units was

$$C_I = 3A\sigma_x\sigma_y / [2(d_{granule}/2)^3]. \tag{3.4}$$

After accounting for pixel size, the units of C_I were CU/μm.

3.4 Results

3.4.1 Observed Background Fluctuations were Spatially Uniform

In the dye transfer experiments, large fluctuations in intensity were seen over time. The mean intensity was calculated for the entire area of a fluorescence recording, as well as for a region of interest containing the vesicles (Fig. 3.6A) and a region of interest not containing the vesicles (Fig. 3.6B). The intensity fluctuations

were largely uniform across the image area (Fig. 3.6C), indicating that they were due to fluctuations in background intensity. Therefore, the frame-by-frame background subtraction performed by the template-matching algorithm in determining the values of Scale should effectively remove these fluctuations.

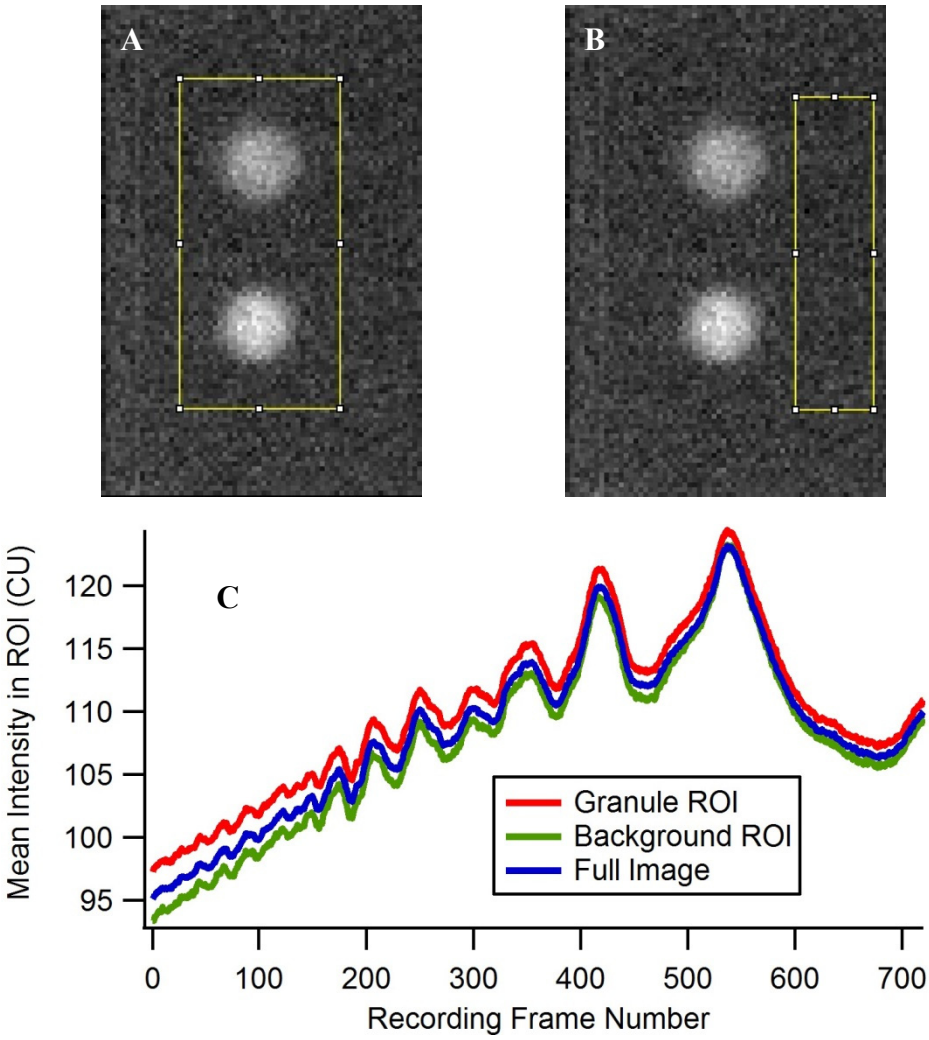

Figure 3.6. Fluctuations of background intensity. A: A region of interest containing the vesicles. B: A region of interest not containing the vesicles. C: The overall fluctuations in intensity over the course of a recording in each of Panel A and Panel B, as well as in the entire image. The fluctuations occur uniformly across the image. The convergence of the mean intensities of the ROIs with time is expected due to photobleaching of the vesicles.

3.4.2 Dye Transfer Data Shows Rapid Photobleaching

Fig. 3.7 shows an example of the calculation of C_I over time for a vesicle pair. Panel A shows the Scale parameter vs time for the fixed (red trace) and moveable (blue trace) vesicles. The insets show the first and last frames of the fluorescence recording, and the boxes show the region that was used as a template for tracking the fixed (red box) and moveable (blue box) vesicles. Panel B shows the intensity profiles of a 3 pixel-wide cross section of the fixed (red trace) and moveable (blue trace) vesicles, along with 2D Gaussian fits. The Panel B insets show the 3D Gaussian fits to the fixed (red box) and moveable (blue box) vesicles in the first frame of the recording, when the vesicles were well separated. The vesicle intensity distributions were well described by Gaussian fits. Panel C shows the C_I traces for the fixed (red trace) and moveable (blue trace) vesicles. A typical value of the RMS noise in the C_I trace was 0.224 CU/μm.

For each vesicle pair, the C_I vs time trace for the fixed vesicle was fit with an exponential and the decay rate, τ, was determined (Fig. 3.8). This was not done for the movable vesicles because they were subjected to more movement, and their apparent intensities could be affected by small variations in the intensity of the excitation light. Two dye transfer tests were excluded from this analysis, one because vesicle intensity was already very low and no decay was apparent, and the other because the decay did not last long enough for a good fit.

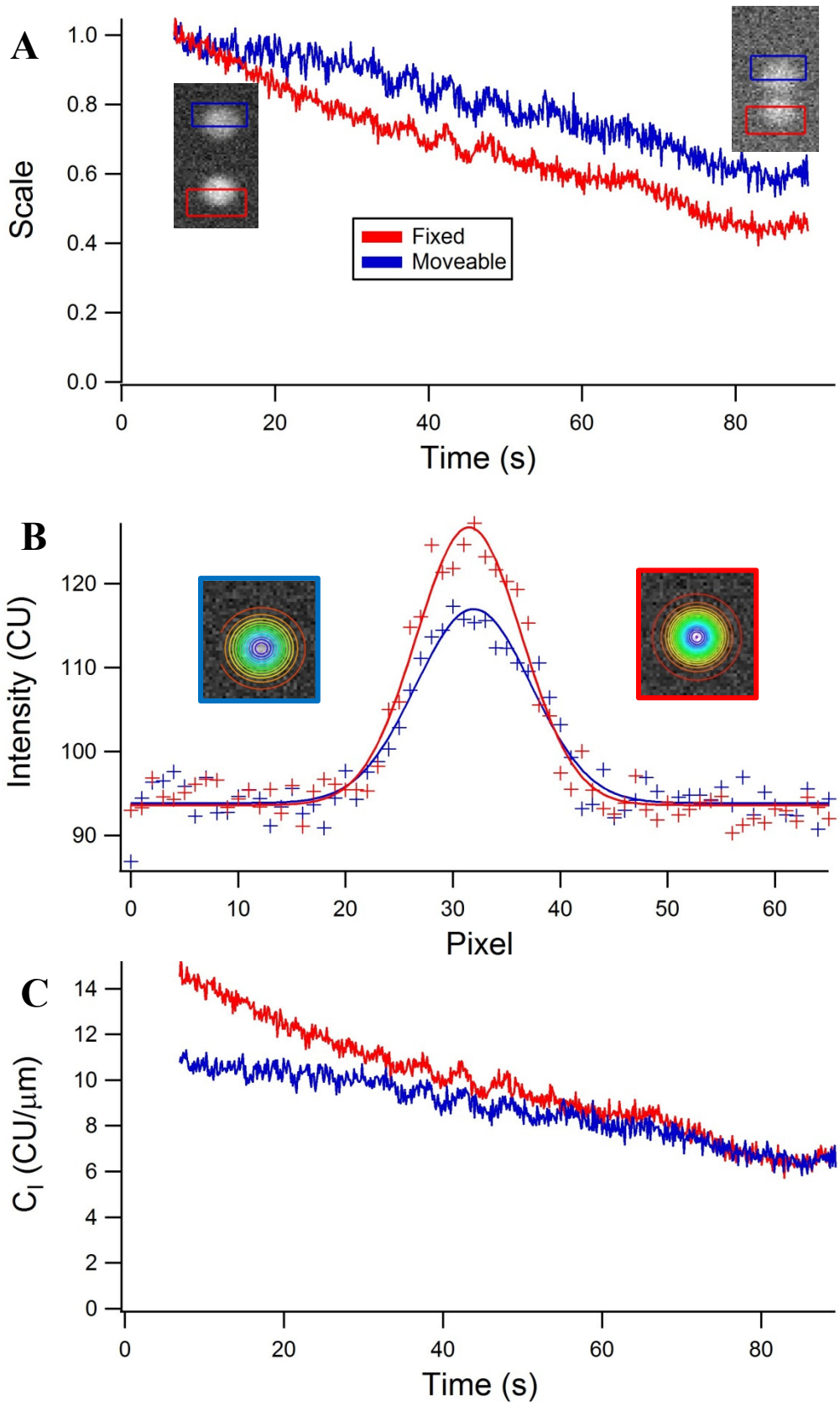
A
Scale
1.0
0.8
0.6
0.4
0.2
0.0
0
20
40
60
80
Time (s)
Fixed
Moveable
B
Intensity (CU)
120
110
100
90
0
10
20
30
40
50
60
Pixel
C
C_I (CU/μm)
14
12
10
8
6
4
2
0
0
20
40
60
80
Time (s)

Figure 3.7. Measuring vesicle intensity over time. A: Plot of the Scale factor vs time for a pair of vesicles. The images show the first and last frames of the recording, with the blue and red boxes indicating the locations of the movable vesicle and fixed vesicle template, respectively. B: Intensity profile of a cross section of each vesicle in the first frame of the recording, and 2D Gaussian fits to the profiles. Since the profiles were fit well by the Gaussians, a 3D Gaussian fit was performed on each vesicle, shown in the insets. C: C_I vs time for the vesicles, determined by multiplying scale factor by initial C_I for each vesicle.

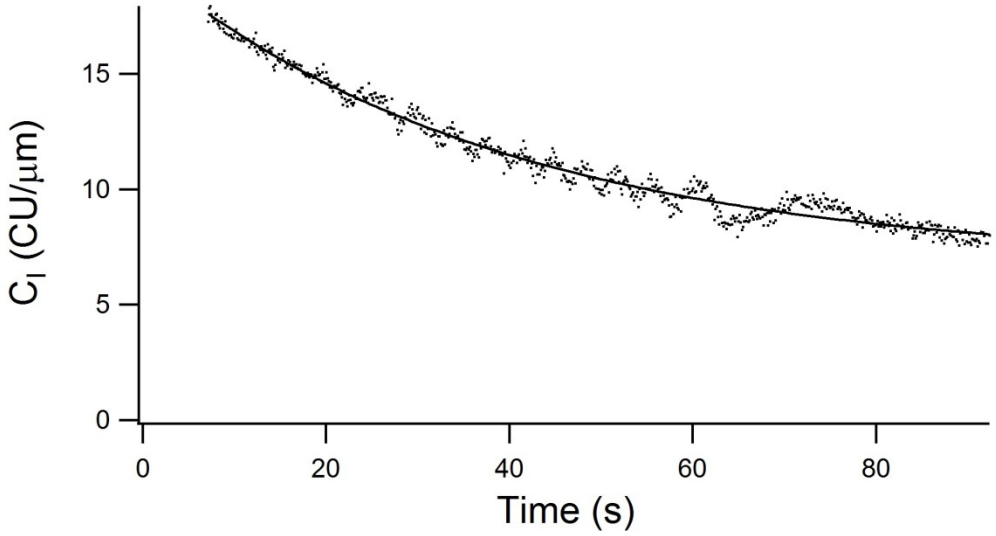

Figure 3.8. Decay of C_I over time for a vesicle. C_I vs time trace for the fixed vesicle from Fig. 3.7C, along with an exponential fit. The fit yielded a τ value of 39 s.

The mean of all 22 bleaching time constants was 39 ± 19 s (mean ± sd). However, vesicles that started with very low intensity had much more widely distributed τ values due to low signal-to-noise ratio. When only the 13 experiments for which the initial C_I value was above 15 CU/μm were used, the mean was 33 s, with standard deviation 9 s.

3.4.3 Preliminary Vesicle-Vesicle Dye Transfer Measurements

Some of the vesicle-vesicle pairs did not directly touch each other due to intervening material (presumably parts of the cytoplasmic matrix.) Those that touched

showed a wide range of binding strength, with some being dissociated at pull forces < 15 pN and some not dissociating with pull forces up to 30 pN, as expected from previous vesicle-vesicle pulling experiments using optical traps[2].

Fig. 3.9 shows two examples of dye transfer tests in which the vesicles bound tightly to each other. In panel A, the C_I of the fixed vesicle (red trace) and moveable vesicle (blue trace) equilibrate over time. Panel B shows the ratio of the moveable vesicle C_I to the fixed vesicle C_I from Panel A (green trace), which starts at a value < 0.8 and increases to ~ 1. The pull force (black trace) increases in steps over time up to ~ 30 pN without dissociation of the vesicle-vesicle bond. Although Fig. 3.9 A,B shows equilibration of CI between two vesicles, the equilibration does not appear to be due to dye transfer. In the case of dye transfer, the vesicle intensities should only equilibrate after the vesicles make contact. However, in Fig. 3.9 A,B, much of the equilibration occurred before the vesicles made contact. Therefore, the equilibration is likely due to variations in the intensity of the excitation light within the field of view, and possibly differential photobleaching. Panels C and D show a different vesicle pair, in which C_I did not equilibrate. This pair bound more weakly, and did not dissociate during 20s at a pull force of ~13 pN, but dissociated rapidly when the pull force increased to > 25 pN. In this case, the two vesicles retain very different C_I values throughout the experiment as expected for unfused vesicles.

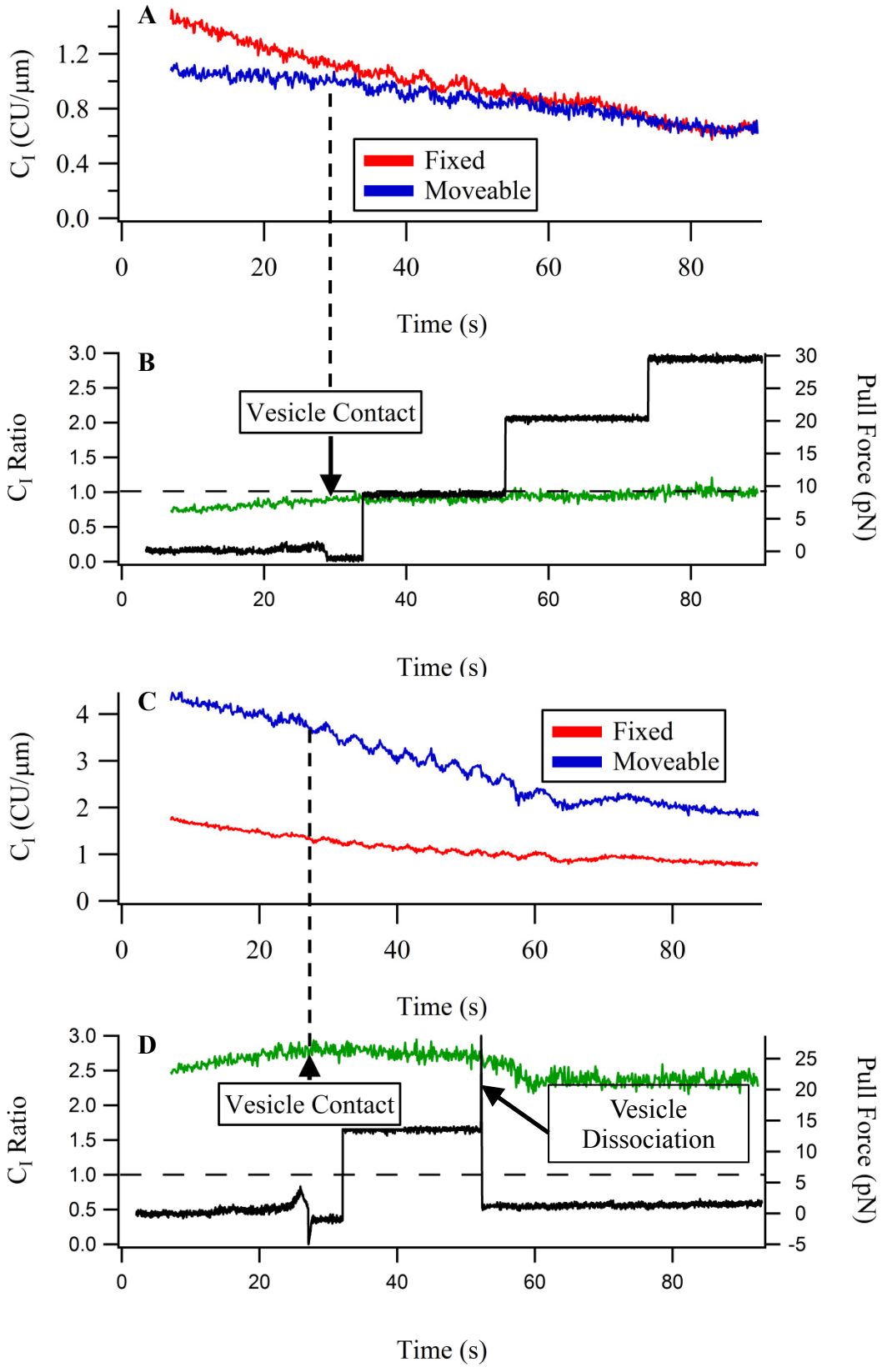
A
B
C
D
Fixed
Moveable
Vesicle Contact
Vesicle Dissociation
C_I (CU/µm)
C_I Ratio
Pull Force (pN)
Time (s)

Figure 3.9. Examples of dye transfer tests. A: C_I traces for the fixed (red trace) and moveable (blue trace) vesicles. B: Ratio of C_I for the moveable vesicle to C_I for the fixed vesicle (green trace), and pull force (black trace). C,D: C_I traces and pull force for a separate vesicle pair. The C_I traces for the vesicle pair in panels A and B equilibrate, but much of the equilibration occurs before the vesicles make contact.

3.5 Discussion

A procedure to measure dye transfer between two vesicles in a dual optical trap has been implemented. Among vesicles that touched directly and bound to each other, some bound weakly enough to be dissociated at pull forces < 15 pN, while others could not be dissociated at pull forces > 30 pN. Notably, although full dissociation events were observed in the vesicle-vesicle pulling experiments, no partial extension events were observed, as in AFM pulling experiments on neurosecretory vesicle-plasma membrane tethers in PC12 cells (chapter 5), which showed few full dissociation events even at pull forces up to 900 pN. These differences are consistent with one physical tether, such as the HOPS complex[1], being responsible for vesicle-vesicle tethering in horse eosinophils while a different tether, such as the exocyst complex, is responsible for neurosecretory vesicle-plasma membrane tethering in PC12 cells (chapter 5).

The intensity profiles of the fluorescing vesicles were well approximated by Gaussian fits, and the total fluorescence intensity per volume of each vesicle was quantified over time. Different C_I values were retained upon contact between vesicles that could then be separated from each other by the trap. For vesicles that bound too strongly to be separated by the trap, trials with sufficiently different C_I values at time of contact were not obtained, perhaps due in part to the rapid photobleaching observed

during experiments. To investigate the photobleaching, the intensities of single, stationary fluorescing vesicles could be measured over time to determine if a characteristic rate of photobleaching and final C_I are observed, providing a control for comparison with photobleaching rates in dye transfer experiments. Further data collection should yield vesicle pairs that both bind strongly and have sufficiently different C_I values at contact for detection of dye transfer.

REFERENCES

1. James, D. J. & Martin, T. F. J. CAPS and Munc13: CATCHRs that SNARE Vesicles. *Front. Endocrinol. (Lausanne).* **4,** 187 (2013).

2. Valero, V., Nevian, T., Ho, D. & Lindau, M. Tethering forces of secretory granules measured with optical tweezers. *Biophys. J.* **95,** 4972–4978 (2008).

3. Hafez I Lindau M,, S. A. Compound exocytosis and cumulative fusion in eosinophils. *J. Biol. Chem.* **278,** 44921–44928 (2003).

4. Fernández-Busnadiego, R. *et al.* Cryo-electron tomography reveals a critical role of RIM1α in synaptic vesicle tethering. *J. Cell Biol.* **201,** 725–740 (2013).

5. Yu, I.-M. & Hughson, F. M. Tethering factors as organizers of intracellular vesicular traffic. *Annu. Rev. Cell Dev. Biol.* **26,** 137–156 (2010).

6. Haugland, R. P., Gregory, J., Spence, M. T. Z. & Johnson, I. D. *Handbook of fluorescent probes and research products*. (Molecular Probes, 2002). at <http://books.google.com/books?id=HagKAQAAMAAJ>

7. Felgner, H., Müller, O. & Schliwa, M. Calibration of light forces in optical tweezers. *Appl. Opt.* **34,** 977–982 (1995).

CHAPTER 4

A COMBINED AFM/TIRF METHOD TO STUDY VESICLE-PLASMA MEMBRANE TETHERING

4.1 Abstract

Various proteins have been implicated in secretory vesicle tethering, but the identity and mechanical properties of the components that form the physical vesicle-plasma membrane link remain unknown. To characterize the nanomechanical properties of secretory vesicle-plasma membrane tethers a novel method was developed, combining atomic force microscope (AFM) force clamp recordings and total internal reflection fluorescence (TIRF) microscopy on membrane sheets from PC12 cells expressing the vesicle marker ANF-eGFP. The attachment of the AFM tip with a vesicle was identified by TIRF imaging and pulling forces applied to record the response of the vesicle-plasma membrane tether. Force clamp recordings revealed tether extensions composed of multiple steps with variable length. The method provides a versatile means of measuring the mechanical and properties of vesicle-plasma membrane tethers and their regulation, and may help to identify the physical vesicle-plasma membrane tether.

4.2 Introduction

The fusion of secretory vesicles with the plasma membrane occurs from a tethered state, in which the vesicles are associated with the plasma membrane via

long-range interactions that do not require the cytoskeleton[1]. However, the molecular identities and their nanomechanical properties are still not known[2].

Multiple protein complexes have been implicated in exocytosis. Among them are long coiled-coil proteins and multi-subunit tethering complexes (MTCs)[1]. Many MTCs contain CATCHR (Complex Associated with Tethering Containing Helical Rods) domains, characterized by an extended rod-like structure composed of helical bundles[1,3]. Among the CATCHR proteins that have been implicated in exocytosis of neurosecretory vesicles is the exocyst complex. If this protein complex forms the physical vesicle-plasma membrane link, then the application of force to a tethered vesicle should lead to stepwise unfolding of its domains.

AFM force clamp experiments on reconstituted or isolated proteins result in stair-step patterns in which each step corresponds to the unfolding of a single domain, and more mechanically stable proteins take longer to unfold[4]. Optical trap pulling experiments on reconstituted SNARE proteins successfully stabilized a half-zippered state of the SNARE complex and measured the extension change related to zippering of different domains[5]. Since the molecular identities of the proteins that form the physical tether between neurosecretory vesicles and the plasma membrane is still unknown, we used an AFM to apply a force clamp directly to secretory vesicles tethered to plasma membrane sheets prepared from PC12 cells using a sonic pulse[6,7], and measured the length and frequency of extension events. Total internal reflection fluorescence (TIRF) microscopy was used to identify a vesicle attached to the AFM tip and to track its movement within the TIRF evanescent wave. Stepwise tether extensions of various lengths were observed, and some of the extensions were

correlated with TIRF intensity changes, indicating they were extensions of the vesicle-plasma membrane tether.

4.3 Methods

4.3.1 Preparation of PC12 Cell Membrane Sheets

Glass-bottomed dishes suitable for TIRF excitation were constructed from 35mm Petri dish lids (#430588, Corning Inc., Corning, NY), into the center of which a 20mm diameter hole was precision cut. A #1.5 30 mm diameter coverslip (64-1499, Warner Instruments, Hamden, CT) was attached to the lid using an RTV615 Silicone Potting Compound kit. To achieve good adhesion of the cell membranes to the surface, a Poly-D-lysine (PDL) coating was applied. 500µL of 0.1% PDL solution (Poly-D-lysine hydrobromide, P7280, Sigma-Aldrich, St. Louis, MO) was pipetted onto the center of a UV-sterilized coverslip, and allowed to incubate for one hour. The dish was then rinsed with sterile H_2O and air dried for 20 minutes. PDL-coated coverslips were stored at 4ºC for up to 7 days.

PC12 cells expressing atrial natriuretic factor linked to eGFP (ANF-eGFP)[8] were obtained from Dr. Ronald Holz, Department of Pharmacology, University of Michigan Medical School. Cells were cultured in F12-K Nutrient mixture with L-Glutamine (21127, Gibco, Life Technologies, Carlsbad, CA) supplemented with 15% horse serum (16050, Gibco), 2.5% Fetal Bovine Serum (10082, Gibco), and 1% Penicillin-Streptomycin-Glutamine 100x (10378, Gibco). To plate the cells in the glass-bottomed dishes, the cells were counted using a Fuchs-Rosenthal chamber and diluted with culture medium to attain an approximate density of $1.6 – 1.9 \times 10^6$

cells/mL. 500µL of this cell suspension was pipetted onto the center of the PDL-coated coverslip. The cultures were incubated at 37ºC, 5% CO_2 for 3 hours. 3mL of growth medium was pipetted into each plated culture. The cells were then allowed to adhere for another 24 hours.

Immediately prior to experiments, the culture medium was replaced by a buffer containing 120mM K-glutamate, 20mM HEPES, 20mM K-acetate, 2mM EGTA, 2mM mgATP, and 0.5mM DTT, pH adjusted to 7.2 with KOH. The cells were then lysed by a 0.1 s, 20 kHz sonic pulse using a Digital Sonifier 250 (Branson Ultrasonics Corporation, Danbury, CT), with amplitude control at 30%, leaving the cytoplasmic face and associated secretory vesicles exposed[6,7]. The lysing buffer was removed to wash out debris, and fresh buffer was added.

To label membrane sheets, the styryl dye FM 4-64 (T-3166, Invitrogen, Carlsbad, CA) was added at a final concentration of 0.5 µM after the above steps. The FM 4-64 dye was not used in the experiments in which AFM data were collected.

4.3.2 TIRF Microscopy

For TIRF imaging, an eclipse microscope with a TI-TIRF-E Motorized Illuminator Unit and APO TIRF 100x 1.49NA oil immersion objective (TIRF) (Nikon Corporation, Tokyo, Japan) was used. TIRF images were recorded with a water-cooled iXon EM+ EMCCD camera (Andor Technology, Belfast, Northern Ireland) with 16 µm x 16 µm pixel size. Accounting for the 100x objective, the pixel size of images recorded by the iXon camera was approximately 160 nm x 160 nm. Andor Solis software recorded the images captured by the iXon camera. The FIRE output of

the iXon camera was connected to the "Aux IN" BNC input of the AFM controller and recorded to establish a time correlation between AFM recording and fluorescence images in the analysis. A KP-D250 camera (Hitachi, Tokyo, Japan) was used to visualize the sample and AFM cantilever under bright field illumination, as well as the AFM laser reflection from the cantilever. This was useful for alignment of the AFM laser on the cantilever and for achieving the necessary relative positioning of the cantilever, membrane sheets, and TIRF objective.

The TIRF microscope was equipped with multiple sets of filters from Semrock (Rochester, NY.) For imaging of eGFP excited by a 488 nm Argon-Ion laser (35-LAP-321-120, Melles Griot, Rochester, NY), the following filter set was used: excitation filter FF01-482/18, emission filter FF01-525/45, dichroic Di01-R488. This filter set was also used for bright field illumination. For imaging FM 4-64 excited by a 561 nm diode-pumped solid state laser (CL561-025-O, CrystaLaser, Reno, NV), the following filter set was used: excitation filter FF01-561/14, emission filter FF01-609/54, dichroic Di01-R561. For visualization of the AFM laser reflection from the cantilever, the following filter set was used: excitation filter FF01-390/40, emission filter BLP01-R405, dichroic Di01-R405.

4.3.3 AFM Apparatus

A 5500 Scanning Probe Microscope (AFM) (Agilent Technologies, Santa Clara, CA) was mounted on the TIRF using an Agilent 5500 ILM Quick Slide stage (Fig. 4.1). Agilent's PicoView 1.15 beta software with a custom-written Python script was used for AFM control and data acquisition. The AFM included a piezoelectric

servo for fine control of cantilever z position. A position sensor and closed loop feedback corrected for hysteresis.

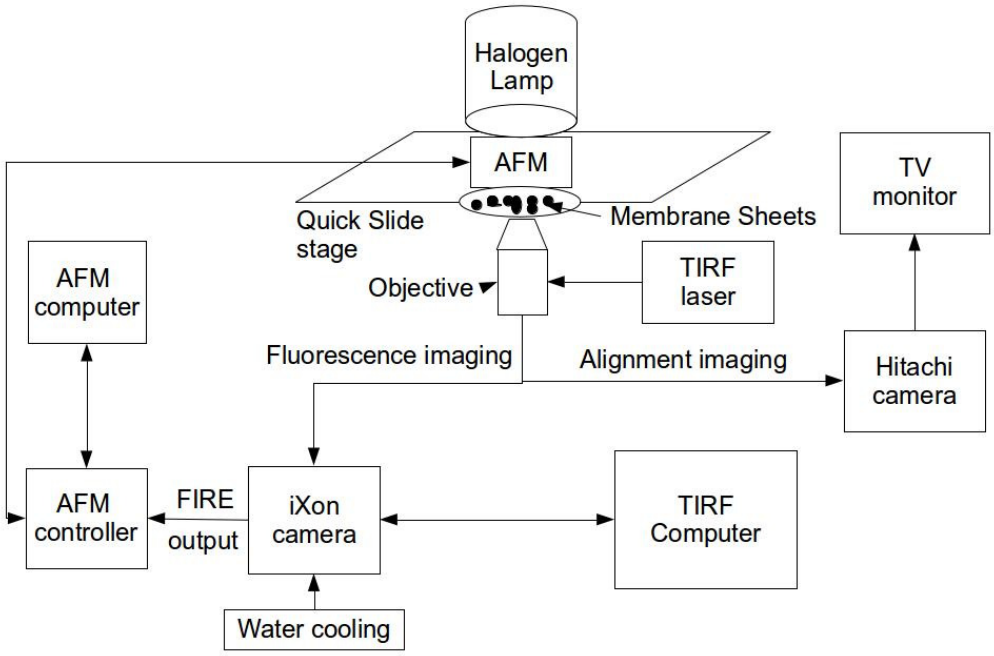

Figure 4.1. Diagram of the apparatus.

4.3.4 Alignment of AFM Laser and Cantilever Calibration

The cantilevers used were Bio-Levers (Olympus, Tokyo, Japan), obtained from Asylum (BL-RC-150VB, Flushing, NY). Asylum reports the Bio-Lever tip radius as ~25±12 nm. For comparison, the radius of PC12 secretory vesicles is ~60 nm[6,9]. The degree of cantilever bending was measured by a laser that was reflected off of the cantilever and onto a quad photodiode (QPD), producing the cantilever deflection signal, V_{defl}. At the beginning of each day of experiments, the AFM laser was aligned

on the cantilever such that it was reflected to the approximate center of the (QPD) that measured V_{defl}. This was done in buffer on the AFM/TIRF assembly using the 405 filter set and Hitachi camera to show the position of the AFM laser on the cantilever. To convert V_{defl} into a pull force, two calibrations were required: deflection sensitivity (D) and cantilever spring constant (k).

D relates the physical cantilever deflection to the voltage signal of the quad photodiode. To measure D, the cantilever was pressed onto the surface of a glass coverslip as used for experiments in the presence of buffer but without PDL or cells on it. Thus, the tip would remain fixed while z was adjusted, causing the cantilever to deflect. Fig. 4.2 illustrates this procedure and the resulting V_{defl}. A plot of V_{defl} vs z shows a straight line for the region in which the tip is pressed onto the surface, and the slope of that line is $-1/D$. The slope was measured with a procedure built into the PicoView software. Values could depend on cantilever properties and exact alignment of the AFM laser, and ranged from 33 to 67 nm/V

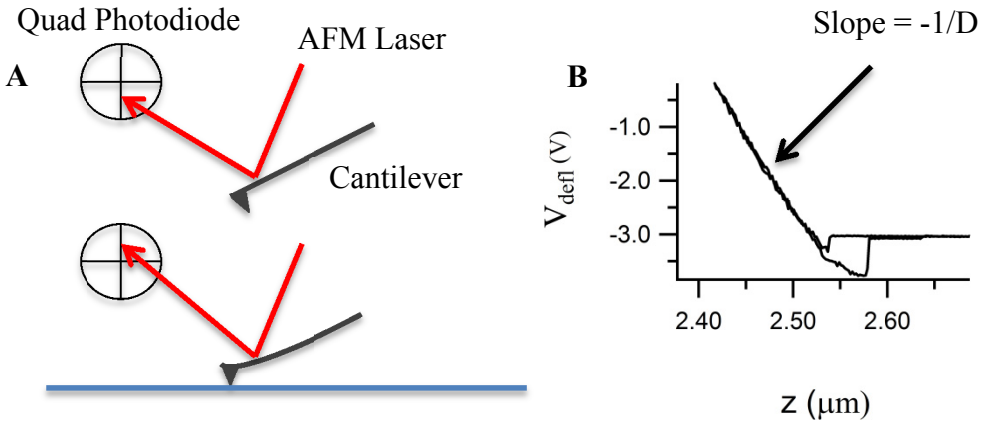

Figure 4.2. Deflection sensitivity calibration. Panel A: The cantilever is deflected as it is pushed onto a hard surface, changing the angle of the reflected beam of the AFM laser such that it strikes a different spot on the QPD. Panel B: The slope of V_{defl} vs z provides the value of D. The cantilever tip is pressed down onto the surface and

then retracted, resulting in the appearance of two traces, one recorded as the tip is pushed down, and the other recorded as the tip is retracted.

To determine *k*, the "Thermal k method" [10] was utilized, as described in section 2.3. In this work, PicoView's proprietary built-in Thermal k method was used, which isolates and fits the portion of the power spectral density of the cantilever oscillations due to thermal excitation (Fig. 4.3). The Thermal k calibration was performed at a height of 50 μm above the same coverslip with buffer that was used for the deflection sensitivity calibration. To minimize mechanical noise in the power spectrum, the thermal k calibration was performed with the iXon camera water cooling pump turned off. Values ranged from 0.008 N/m to 0.04 N/m, consistent with the nominal spring constant range of 0.009 – 0.1 N/m, with a typical value of 0.03 N/m. Both *D* and *k* were calibrated independently for each cantilever used.

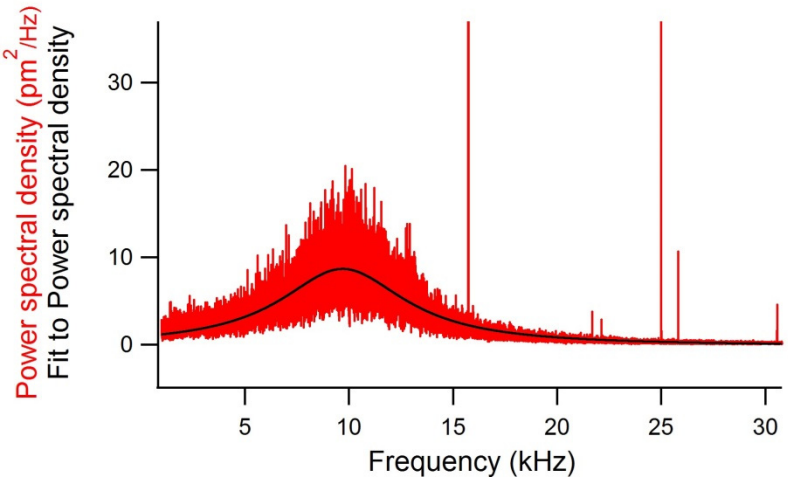

Figure 4.3. PSD of thermal vibrations of a cantilever and fit.

4.3.5 Alignment of Membrane Sheets, TIRF Objective, and AFM Cantilever

Immediately after cell lysis, the coverslip with the membrane sheets was mounted on the AFM, which was slid into place over the TIRF objective using the Quick Slide stage. The halogen lamp was turned on, and the Hitachi camera was used along with a 4x objective and the 488 filter set to observe the cantilever and the lysed region of the sample, where the membrane sheets were located. The lysed region was recognizable by absence of cells. Micrometers on the AFM stage were then adjusted by hand to position the sample so that the lysed region was located below the cantilever tip, and micrometers on the Quick Slide stage were used to center the AFM tip in the TIRF microscope field of view.

A motor was then used approach the sample surface using the PicoView software. Contact with the sample surface was indicated by V_{defl} exceeding a preset threshold. The AFM tip was re-centered in the field of view, using the micrometers on the Quick Slide stage. The 4x objective was switched out for a 40x objective, and the AFM tip was centered again. The 40x objective was then switched out for the TIRF objective. Due to the short working distance of the TIRF objective, it was no longer possible to view the AFM tip directly. However, by using the 405 filter set, the light from the AFM laser could be seen. The TIRF objective was raised toward the sample until the shadow of the tip was visible within the laser light. When the shadow of the tip was nearly in focus, the objective was close to the sample. The position of the tip was again centered in the field of view, and then the illumination source was changed to the 488 nm laser with the 488 filter set. The eGFP-labeled vesicles were visible in

the TIRF illumination. The shadow of the AFM tip could also be seen by allowing a small amount of transmitted light from the microscope's halogen lamp.

The cantilever tip was moved to a new spot away from the original landing spot in case the sample was damaged by the coarse AFM approach. To do this, the AFM servo was used to lift the cantilever 1 μm off the surface, and the AFM micrometers were used to move the sample without moving the cantilever. Once a membrane sheet was located, the tip was positioned over it. The alignment was typically completed within 15 minutes after the time of PC12 cell lysis.

4.3.6 Force Clamp Procedure

Fig. 4.4 illustrates the force clamp procedure, much of which was automated with the custom Python script. During the approach and push phases, V_{defl}, servo position, and the iXon camera FIRE signal were all recorded using the Python script at a rate of ~7 Hz. During approach, the cantilever was stepped towards the surface in 6 nm increments until the measured cantilever deflection voltage, V_{defl}, increased by 0.05V above the initial value, indicating that the cantilever was pressing into the surface. To ensure that the tip was in contact and that the change in V_{defl} was not due to signal drift that was observed to occur both with servo height and with time, the script continued the cantilever approach until two V_{defl} increases of 0.05 V occurred within 50 nm of vertical displacement. These parameters were determined by trial and error to be reliable indicators of surface contact. The approach was performed under TIRF imaging, with the iXon camera acquiring in frame transfer mode with 50 ms exposure times. Approach times were generally <30 s, but varied widely.

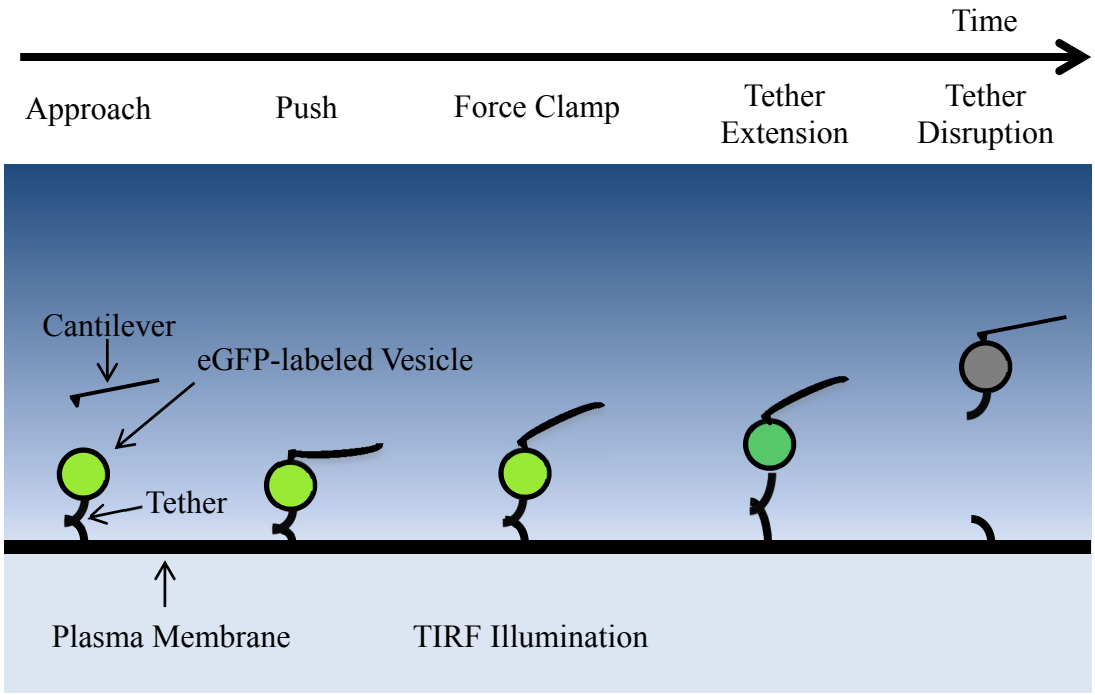

Figure 4.4. Force clamp procedure. Steps of a force clamp experiment are shown from left to right. First, the cantilever approaches the membrane sheet. After contact, the cantilever tip maintains a push force and binds nonspecifically to a vesicle on the surface as shown here or alternatively the cytoplasmic face of the plasma membrane sheet. The cantilever then applies a pull force (force clamp), which can result in unfolding or disruption of vesicle-plasma membrane tethers. Increases in vertical position of vesicles within the TIRF evanescent wave result in decreases in fluorescence intensity. Figure not to scale. The cantilever tip radius is approximately half of a vesicle radius.

Once the cantilever was in contact with the surface, the push phase was initiated, in which the cantilever could bind nonspecifically to the cytoplasmic face of the membrane sheet or to a vesicle on the surface. The EMCCD image acquisition was terminated, and the cantilever was maintained at constant V_{defl} until a new acquisition was initiated.

In the force clamp phase, the cantilever was retracted to apply 4 different pulling forces of increasing magnitude sequentially, each for 12.5 s. Tether extensions and disruptions could be detected as changes in servo position. If a vesicle moved

vertically within the evanescent wave, this movement could simultaneously be detected as a decrease in fluorescence intensity. During this phase, the cantilever deflection V_{defl}, servo position z_{servo}, and the iXon camera FIRE signal were all recorded at a 5 kHz data rate. The V_{defl} data were later smoothed using Igor Pro's box algorithm over 83 points (1/60 s) to remove line frequency noise. The EMCCD image acquisition ended shortly before the last pull force segment ended. Finally, after the last force clamp segment ended, the servo position was adjusted to 500nm above the position where surface contact was detected during the approach, and a final deflection and time value were recorded.

4.3.7 Synchronization of AFM and TIRF Data

For analysis, the recorded V_{defl}, z_{servo}, and camera FIRE signal traces were imported into Igor Pro. During the approach phase, the time resolution of the recording of the FIRE signal was not sufficient to resolve individual camera frames. Therefore, the camera frames were evenly spaced within the timeframe that the camera was recording. Using the known cycle time of the camera (in this case 0.05091s), the frame number of the first full frame captured during the force segments, and the start time of that frame, the gap between the end of the script data recording and the beginning of the force clamp segments was determined.

During the force clamp phase, the time resolution of 5 kHz allowed greater precision. A custom Igor function scanned the FIRE signal record (Fig. 4.5. red trace). If a point had a value < 3 V, the camera was considered to not be exposing, otherwise, the camera was exposing. Using the fact that the last camera frame was known to be

frame 1000 of the sequence, a new wave, called *fnum*, was generated that had values equal to the current frame number x 10^{-3} at all points for which the camera was exposing and a lower value otherwise (Fig. 4.5, blue trace). This approach directly matched each camera frame exactly to the corresponding deflection and z sensor data.

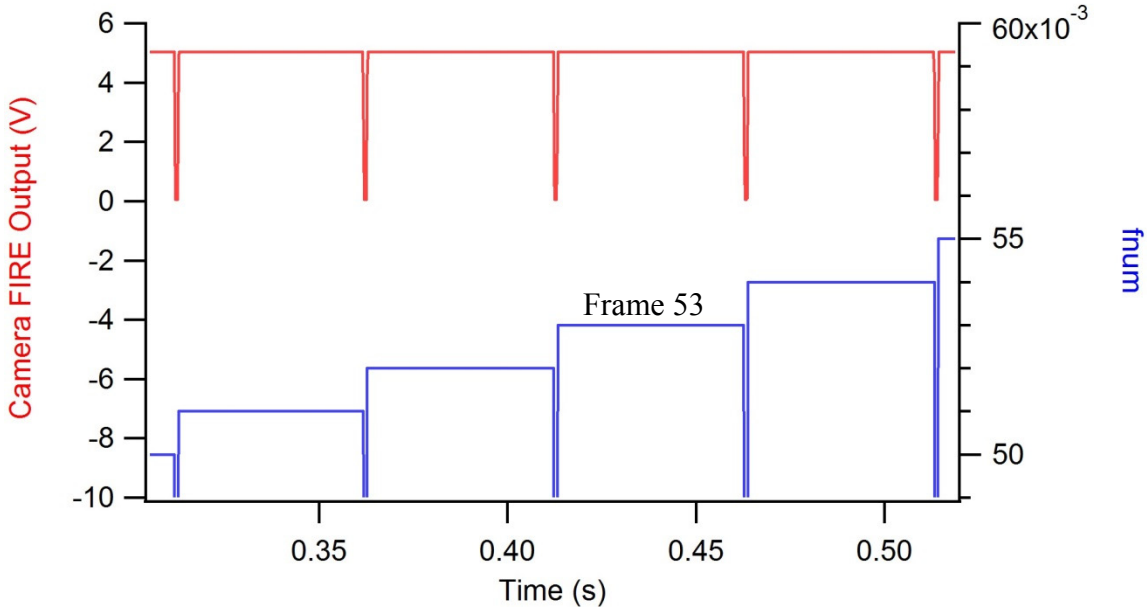

Figure 4.5. The *fnum* trace. The camera FIRE signal was converted to the *fnum* trace, such that the frame number of the TIRF recording was *fnum* × 10^3.

4.3.8 Conversion of Cantilever Deflection to Force

Conversion of the cantilever deflection V_{defl} to force relies on two calibrations: deflection sensitivity (D) and cantilever spring constant (k). The product of D and k gives the conversion factor, C, from V_{defl} to force, such that force F = CV_{defl}. In these experiments, three sources of error in the measurement of applied pull force had to be considered: error in the calibrations D and k, error due to dependence of baseline V_{defl} on the position of the servo that controlled cantilever height (z_{servo}), and error in the

determination of baseline V_{defl} at the sample surface. Baseline V_{defl} refers to the value of V_{defl} when no force was acting on the cantilever.

To determine the error in D, 20 consecutive measurements of D were performed with the same cantilever, and the RMS deviation was determined to be 1.88 nm/V. For the force curve experiments, 5 D values were averaged to determine the value used in the conversion factor, so the final standard error was:

$$\sigma_D = (1.88 nm/V) \cdot 5^{-1/2} = 0.841 \ nm/V . \tag{4.1}$$

The Agilent Thermal k software reported the k value with good reproducibility to the thousandths place in N/m. Therefore, an error of 0.0005 nN/nm was assumed

$$\sigma_k = 0.0005 \ nN/nm . \tag{4.2}$$

such that the total error in C was:

$$\sigma_C = (k^2\sigma_D^2 + D^2\sigma_k^2)^{1/2} . \tag{4.3}$$

To examine the dependence of V_{defl} on z, a subset of 60 of the 390 collected force curves was selected using the random number generator in the program R. Of the 60 force curves chosen, 4 were discarded because they were unusable due to problems that occurred during data collection. For the region of a force curve during which the servo was approaching the surface, linear fits to the V_{defl} vs time trace and the z_{servo} vs time trace were performed. The ratio of the slopes of the fits gave a value for the V_{defl} drift in $V/\mu m$. A histogram of all the V_{defl} drift values was generated that revealed a Gaussian peak. A Gaussian fit to the histogram (Fig. 4.6) provided a drift value of -0.05±0.043 V/μm (mean ± sd). To account for the change of V_{defl} with z_{servo} the V_{defl} values were accordingly corrected:

$$V_{defl,corrected} = V_{defl} + z \times (0.05\,V / \mu m)\,. \tag{4.4}$$

Also, the V_{defl} measurements had an uncertainty of:

$$\sigma_{V_{defl}} = z \times (0.043\,V / \mu m)\,. \tag{4.5}$$

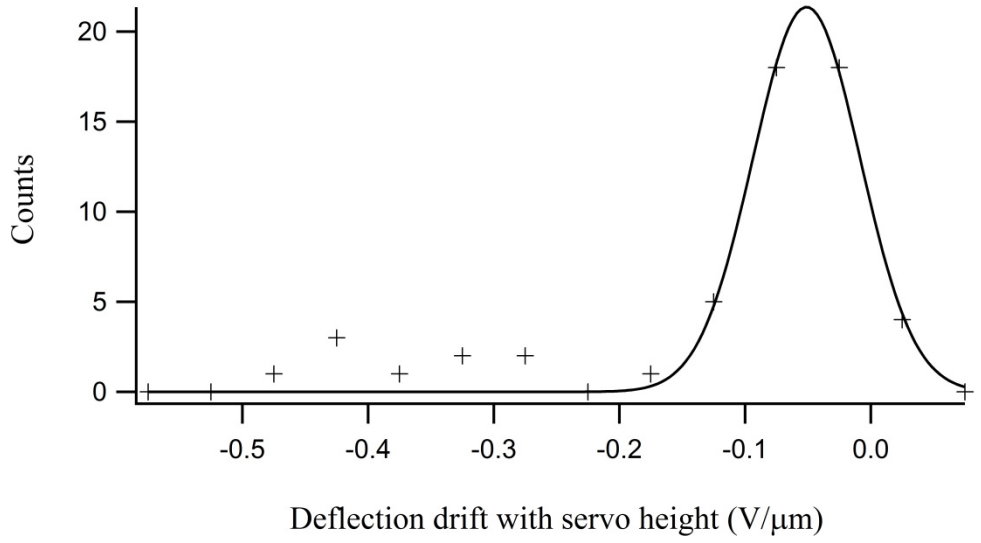

Figure 4.6. Histogram of deflection drifts with servo height (markers) and Gaussian fit. The drift is -0.05±0.043 V/μm. One large drift outlier at -4.78 V/μm is not shown, but it had no significant effect on the fit.

The baseline value of V_{defl} at the sample surface in the absence of force was estimated at both the beginning and the end of each force curve. During cantilever approach, surface contact was identified by an increase of V_{defl} by 0.05 V above the initial value, then a second increase of 0.05 V that occurred with <50 nm further z_{servo} displacement. The second increase was required to confirm contact, but the actual point of contact should almost always occur at the beginning of the first 0.05V increase. Therefore, the V_{defl} at initial contact with the surface was taken to be:

$$V_{surface_i} = V_{contact} - 0.075\,V\,, \tag{4.6}$$

where $V_{contact}$ was the value of V_{defl} at which the script reported confirmed contact with an error:

$$\sigma_{V_{contact}} = 0.025V \,. \tag{4.7}$$

A second estimate of baseline V_{defl} was taken after the servo was set to $z_{contact}$ + *500 nm* at the end of each force clamp recording giving a value V_{end}. In this case, the error was due to the V_{defl} drift with z_{servo}, so the baseline V_{defl} at the surface at the end was estimated to be

$$V_{surface_f} = V_{end} - 0.025\ V \,. \tag{4.8}$$

with an error

$$\sigma_{V_{surfave,f}} = 0.0215V \,. \tag{4.9}$$

In addition to the change of V_{defl} with z_{servo}, V_{defl} was also observed to drift to more negative values with time. To account for this drift, the V_{defl} and time values at surface contact (Eq. 4.6 and Eq. 4.8) at the beginning and end of the run were taken as endpoints for a line, and the slope of that line was calculated. For each pull segment, this slope value was multiplied by the time at the segment center and added to the V_{defl} value of that segment. With the above corrections, the final conversion from V_{defl} to force (F) was:

$$F = -C[V_{defl} + z(0.05V/\mu m) - V_{contact} + 0.075V - \tag{4.10}$$

$$(V_{end} + 0.25V - V_{contact} + 0.075V)/(t_{end} - t_{contact})](t_{segment} - t_{contact}) \,,$$

where F is the pull force value for a given segment, V_{defl} the measured deflection value for the segment, $t_{contact}$ the time at which $V_{contact}$ was measured, t_{end} the time at which V_{end} was measured, and $t_{segment}$ the time at the center of the segment. The minus sign

was used to give pull forces positive values. When the above errors were included, the variance of each force measurement was:

$$\sigma_F^2 = [\sigma_C \frac{F}{C}]^2 + [\sigma_{V_{defl}} C]^2 + [\sigma_{end} C(t_{segment} - t_{contact})/(t_{end} - t_{contact}) \quad (4.11)$$

$$+ [\sigma_{contact} C(-1 + (t_{segment} - t_{contact})/(t_{end} - t_{contact}) .$$

This method of calculating pull forces assumed that the cantilever tip was free of all contact with the surface at the times when $V_{contact}$ and V_{end} were measured. This may not always have been true, and a large error in F could result from a cantilever either beginning or ending a force curve with some deflection due to surface contact. To ensure that such cases were not contaminating the analysis results, segments with outlier F values were excluded.

4.4 Results

4.4.1 Clusters of Vesicles Are Found Only on Membrane Sheets

Plasma membrane sheets with tethered vesicles exposed on the surface were prepared by application of a sonic pulse to ANF-eGFP expressing PC12 cells cultured on glass coverslips. To locate membrane sheets for force clamp experiments, membrane sheets were labeled with 0.5 μM FM 4-64. Like other FM dyes, FM 4-64 partitions into membranes and is highly fluorescent there, whereas its fluorescence is quenched in the aqueous phase[11–14]. FM 4-64 has absorption and emission peaks of 560 nm and 767 nm, respectively, making it suitable for use in cells that also express a GFP construct[13,15]. As shown in the example of Fig. 4.7, not all membrane sheets had vesicles on them, but vesicle clusters were only present on membrane sheets.

Therefore, in the force clamp experiments membrane sheets were identified by the clusters of vesicles on them, without need for FM 4-64 staining.

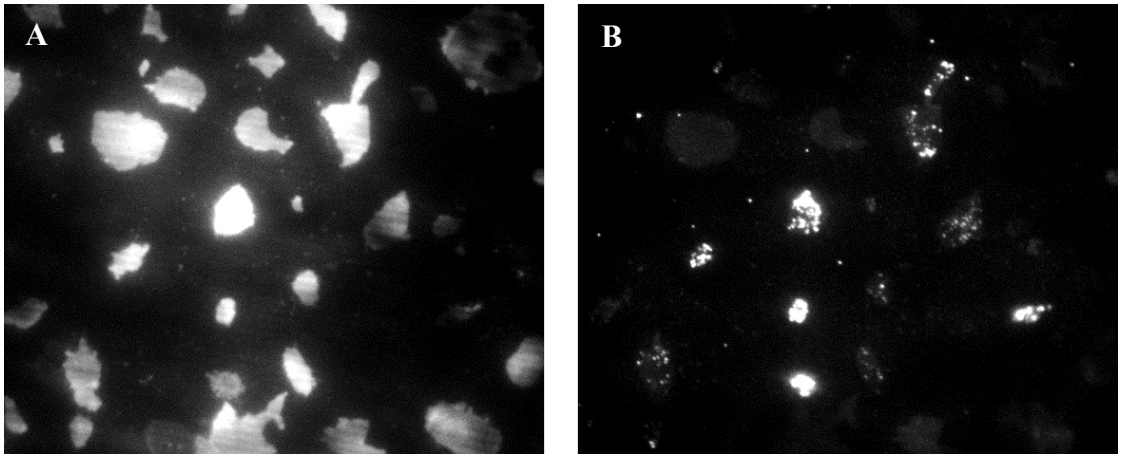

Figure 4.7. Imaging of membrane sheets. Contrast-enhanced image of ANF-eGFP-tagged secretory vesicles on PC12 membrane sheets labeled with FM 4-64 and excited by 561nm (panel A) and 488nm (panel B) laser light in TIRF mode. Panels A and B show the same region of the sample. The 561nm light excites FM 4-64, which labels membrane sheets, while the 488nm light excites eGFP. Not all membrane sheets have vesicles on them, but vesicle clusters are always located on membrane sheets.

4.4.2 AFM/TIRF Recordings Reveal Stepwise Tether Extensions

Fig. 4.8 shows an example of a force clamp experiment to characterize the mechanical properties of vesicle-plasma membrane tethers. Forces between the sample surface and the cantilever tip were recorded as deflection of the cantilever, V_{defl}, (Fig. 4.8, black trace), together with z_{servo} (Fig. 4.8 blue trace) and TIRF fluorescence images.

For each force clamp experiment, the TIRF recordings were examined for evidence of a fluorescent vesicle at the cantilever tip. Insets a-e in Fig. 4.8 are TIRF images of the membrane sheet at different times during the experiment, in which a change in fluorescence intensity was observable. The white boxes enclose a 3x3 pixel

square in which the change was quantified. The average intensity, *I*, of those 9 pixels in every frame of the TIRF image sequence was plotted on the same time axis as the AFM data (Fig. 4.8, green trace).

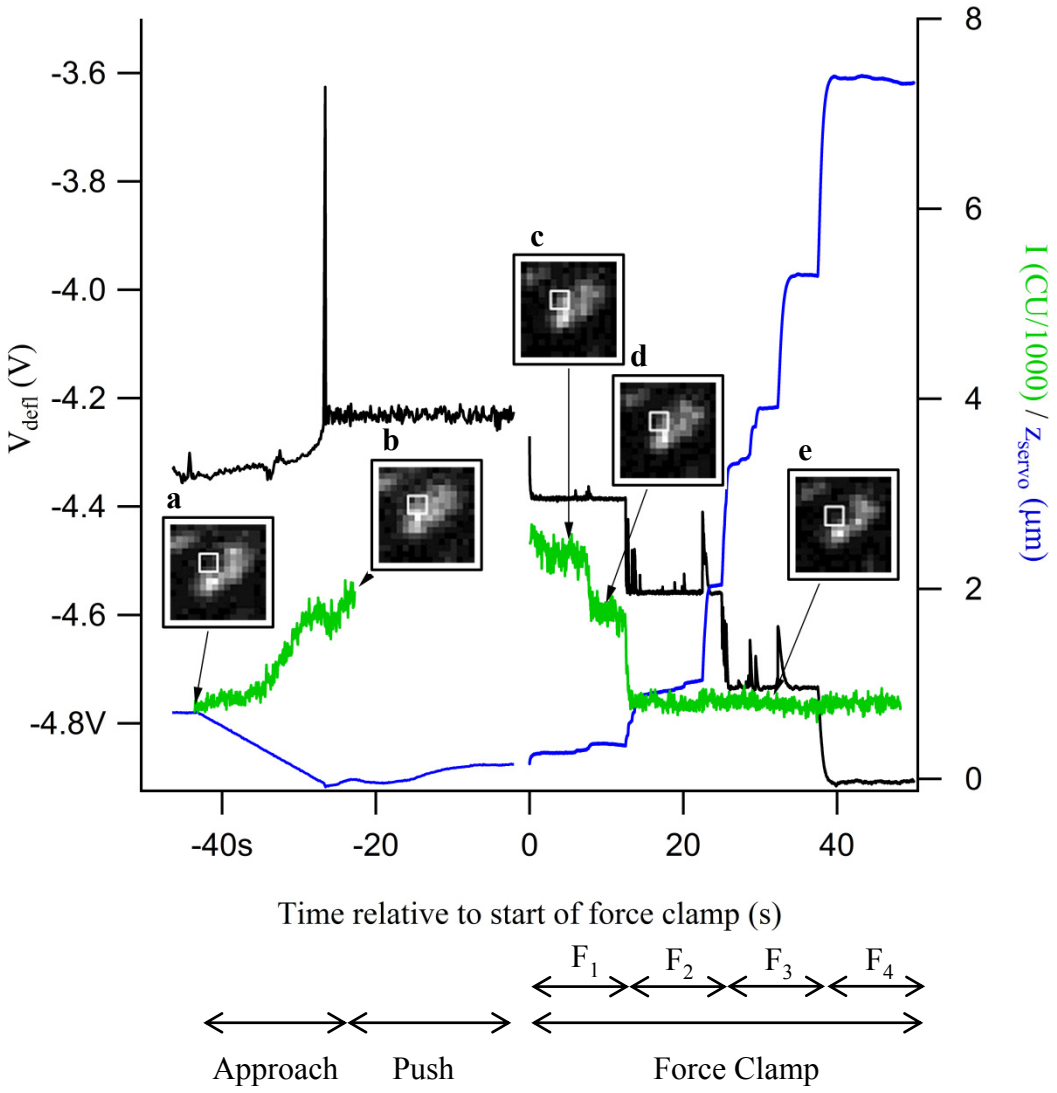

Figure 4.8. Sample of force clamp data. V_{defl} (black), z_{servo} (blue), and *I* (green) are plotted on the same time axis, showing the approach, push, and force clamp phases F_1-F_4 of the experiment. Insets from the TIRF imaging show the fluorescence changes as a vesicle approaches the surface (a,b) with the cantilever tip and is then pulled away (c-e). The green trace shows the time course of the fluorescence intensity in the region marked by the white squares in a-e.

During the approach phase, the AFM servo was lowered (Fig. 4.8, blue trace), and *I* increased (Fig. 4.8, green trace) as the cantilever approached the surface, because in this experiment, a vesicle was already attached to the cantilever tip at the start, presumably picked up in a preceding interaction with the membrane sheet. An increase in V_{defl} occurred (Fig. 4.8, black trace) as the cantilever made contact, followed by a brief spike when control of the z_{servo} position switched from direct position control to automatic feedback control to maintain constant force (constant V_{defl}). The brief spike was limited to 1 data point, and sometimes not seen at all. Given that the data acquisition during the approach phase was ~140 ms per point, the duration of the spike must have been a fraction of that. Once contact had been established, a constant push force was applied by holding V_{defl} constant while the first TIRF image acquisition sequence was stopped and a new acquisition started.

During the force clamp phase of the experiment, 4 different pull forces, F_1-F_4, increasing stepwise in magnitude were applied, each for 12.5 seconds, as indicated at the bottom of Fig. 4.8. Tether extension events appeared as transient spikes in the V_{defl} trace, accompanied by stepwise increases in the z_{servo} trace. When a tether extension event occurred, V_{defl} increased as the cantilever tip was suddenly released and the cantilever deflected upwards, away from the sample surface. To return V_{defl} to the setpoint value, the positioning servo moved the cantilever further away from the surface, causing the increase in z_{servo}. Along with the first few events in segment 1, an associated decrease in *I* occurred (Fig. 4.8, green trace 0..12.5 s, and insets c-e) due to movement of the vesicle away from the surface into a region of lower intensity of the evanescent wave excitation. After the start of segment 2, no further significant change

was seen in *I* because, by the beginning of segment 2, the vesicle had been pulled out of the evanescent wave, leaving only background intensity from other nearby vesicles or ambient sources.

4.4.3 Identification of Vesicle-Plasma Membrane Tether Extensions

Changes in AFM servo z position may not only reflect vesicle-plasma membrane extensions, but could alternatively be due to detachment of the membrane sheet from the surface or due to extensions of the AFM tip-vesicle link. However, the fact that the fluorescence of the vesicles surrounding the vesicle pulled out of the evanescent wave remained unchanged in Fig. 4.8 confirms that the change in *I* corresponded to a vesicle pulled away from the membrane sheet, and not the membrane sheet itself being detached from the surface. On the other hand, extension of the AFM tip-vesicle link would not be associated with a change in the vesicle's TIRF intensity. To compare the change in vesicle z position determined from the change in TIRF intensity with the extension length reported by the AFM servo, the dependence of the vesicle fluorescence intensity $I_{vesicle}$ on the height z above the surface

$$I_{vesicle} = I_{vesicle,0} \exp(-z / d_{TIRF}) \tag{4.12}$$

can be used, where $I_{vesicle,0}$ is the value of $I_{vesicle}$ at z = 0 and d_{TIRF} is the decay length of the evanescent TIRF excitation wave.

The value d_{TIRF} was determined from force clamp experiments in which a vesicle was already attached to the tip during the approach phase (as in Fig. 4.8.) For each individual approach, *I* was plotted vs *z* during the approach, and an exponential

was fit to data showing a continuous increase in I during the approach. The weighted RMS mean and standard deviation of the decay constants obtained from the fits were calculated using the program R, and found to be: d_{TIRF} = 102±34 nm (mean±sd, n = 5), in good agreement with the theoretical estimate $d_{TIRF,theoretical}$ = 94 nm based on the TIRF illumination angle θi = 66.8º.

Before equation 1 could be applied to convert the change in intensity to a change in vesicle height, the background intensity $I_{background}$ had to be subtracted. $I_{background}$ was determined from the baseline level after the vesicle was pulled out of the evanescent wave, which in the example of Fig. 4.8 occurred after the transition from segment 1 to segment 2. If the vesicle moves from a height z_i with intensity I_i to a height z_f with intensity I_f, the change Δz_{TIRF} can thus calculated from the intensities as:

$$\Delta z_{TIRF} = -d_{TIRF} \times \ln \frac{I_f - I_{background}}{I_i - I_{background}} \tag{4.13}$$

Fig. 4.9 shows the servo position change, Δz_{servo} (blue trace), for the events that occurred between insets c and d of Fig. 4.8 along with the extension length calculated from the changes in I, Δz_{TIRF} (green trace).

The late phase of Δz_{servo} starting at ~7.5 s was matched by a corresponding Δz_{TIRF} increase of similar magnitude, whereas the initial Δz_{servo} occurring from ~6 – 7.5 s was not associated with a change in Δz_{TIRF}. We therefore conclude that the initial change in the Δz_{servo} trace did not involve movement of the vesicle, but the later extensions did. The initial Δz_{servo} change thus appears to be related to an extension of the link between AFM tip and vesicle, whereas the later extensions indicate extensions of the vesicle-plasma membrane tether.

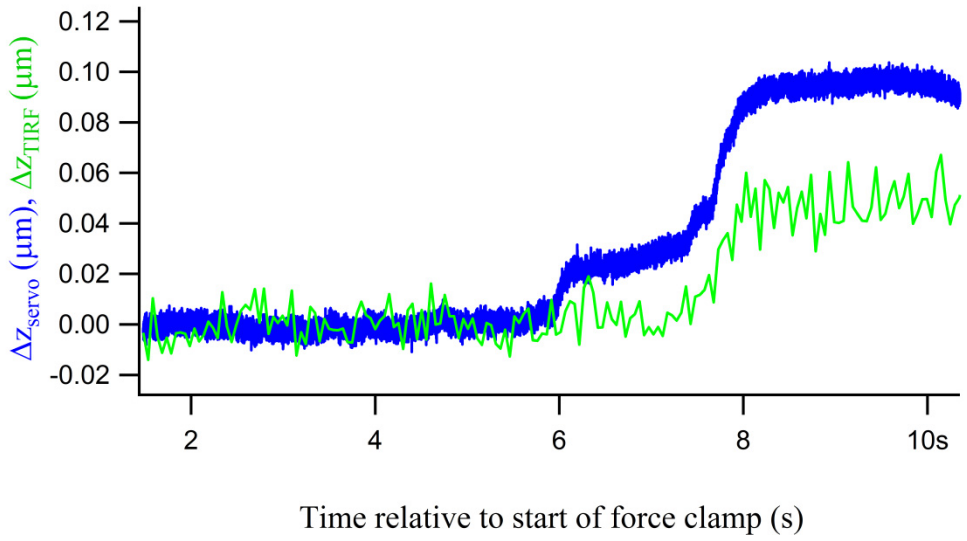

Figure 4.9. Comparison of servo extension and fluorescence intensity change. Extension change due to the events in segment 1 of Fig. 4.8, measured by z servo extension (Δz_{servo}), and by conversion of TIRF intensity (Δz_{TIRF}). A strong correlation between the traces is seen in the later phase, but little correlation with the first change in Δz_{servo}.

4.4.4 Measurement of Event Properties

A subset of individual tether extension events were analyzed in more detail (Fig. 4.10). For each event, AFM servo position change (Δz_{servo}) was measured. To correct for background drift in z, a baseline was fit to the portion of the z trace before the event occurred and projected to after the end of the event. Δz was then taken as the difference between the measured z value and the projected z value. The amplitude of the force transient was also measured. The decay time of the force transient was determined by exponential fit.

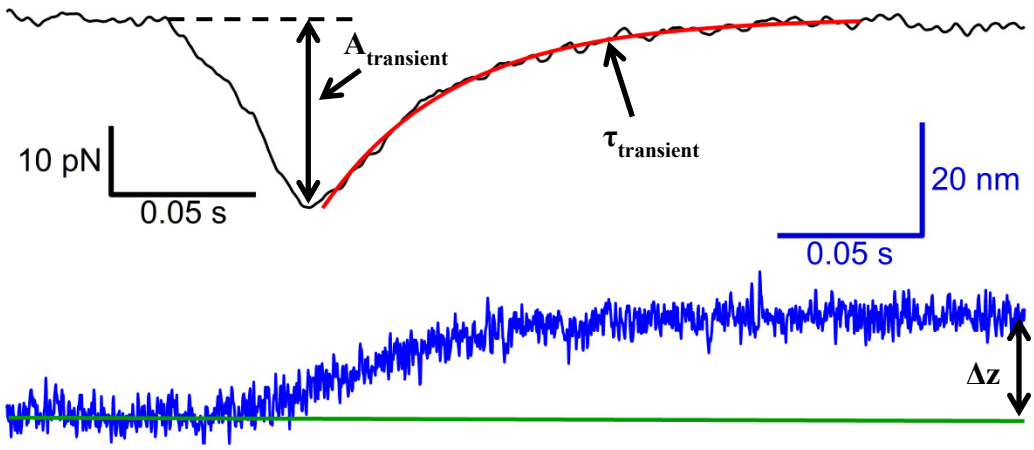

Figure 4.10. Measurement of event properties. The event is characterized by a transient decrease in pull force (black trace) determined from the V_{defl} change and a stepwise increase in z (blue trace). Note that pull force has opposite sign to V_{defl}. The green line is a projection of the baseline of z from before the event to after, and the difference between the projected and observed z values is Δz, in this case 18 nm. The amplitude (Atransient) of the force transient (black trace) was also measured as -26.8 pN. The decay time was determined by exponential fit (red trace) as 48 ms.

4.5 Discussion

Fusion of secretory vesicles with the plasma membrane is preceded by various steps including tethering, docking, and priming[1]. Long tethers (>5 nm) providing a mechanical link between secretory vesicles and the plasma membrane have been observed by electron microscopy[16], but their mechanical properties are unknown. Here, we developed an approach using AFM force clamp measurements on secretory vesicles of ANF-eGFP expressing PC12 cells associated with plasma membrane sheets that revealed stepwise tether extension events. Simultaneous TIRF imaging of the GFP-labeled vesicles allowed direct detection of vesicle displacement during tether extension induced by mechanical force pulling on the vesicle, and some tether

extension events were correlated with vesicle intensity changes, indicating that those events were due to extension of vesicle-plasma membrane tethers.

The method described here is a highly versatile way to directly measure the nanomechanical properties of vesicle-plasma membrane tethers. As shown in chapter 5, the method can be applied to determine if the measured stepwise tether extensions are consistent with sequential unfolding of the exocyst based on its structural properties[17,18]. Comparing measurements in the absence and presence of the non-hydrolysable GTP analog GTPγS will reveal if tether extensions are regulated by GTP binding proteins as expected from biochemical studies[1]. Eventually, comparison of the mechanical and regulatory properties of vesicle-plasma membrane tethers determined using this method with force clamp experiments on the specific proteins and protein complexes implicated in exocytosis can help to identify which candidates possess the properties of the tether. In this way, the proteins that make up the physical vesicle-plasma membrane tether may be identified.

REFERENCES

1. James, D. J. & Martin, T. F. J. CAPS and Munc13: CATCHRs that SNARE Vesicles. *Front. Endocrinol. (Lausanne).* **4,** 187 (2013).

2. Fernández-Busnadiego, R. *et al.* Cryo-electron tomography reveals a critical role of RIM1α in synaptic vesicle tethering. *J. Cell Biol.* **201,** 725–740 (2013).

3. Yu, I.-M. & Hughson, F. M. Tethering factors as organizers of intracellular vesicular traffic. *Annu. Rev. Cell Dev. Biol.* **26,** 137–156 (2010).

4. Bujalowski, P. J. & Oberhauser, A. F. Tracking unfolding and refolding reactions of single proteins using atomic force microscopy methods. *Methods* **60,** 151–160 (2013).

5. Gao, Y. *et al.* Single reconstituted neuronal SNARE complexes zipper in three distinct stages. *Science* **337,** 1340–1343 (2012).

6. Avery, J. *et al.* A cell-free system for regulated exocytosis in PC12 cells. *J. Cell Biol.* **148,** 317–324 (2000).

7. Lang, T. Imaging Ca2+-triggered exocytosis of single secretory granules on plasma membrane lawns from neuroendocrine cells. *Methods Mol. Biol.* **440,** 51–59 (2008).

8. Burke, N. V. *et al.* Neuronal peptide release is limited by secretory granule mobility. *Neuron* **19,** 1095–1102 (1997).

9. Tooze, S. A., Flatmark, T., Tooze, J. & Huttner, W. B. Characterization of the immature secretory granule, an intermediate in granule biogenesis. *J. Cell Biol.* **115,** 1491–1503 (1991).

10. Hutter, J. L. & Bechhoefer, J. Calibration of atomic-force microscope tips. *Rev. Sci. Instrum.* **64,** 1868–1873 (1993).

11. Betz, W. J., Mao, F. & Bewick, G. S. Activity-dependent fluorescent staining and destaining of living vertebrate motor nerve terminals. *J. Neurosci.* **12,** 363–375 (1992).

12. Wu, Y., Yeh, F. L., Mao, F. & Chapman, E. R. Biophysical characterization of styryl dye-membrane interactions. *Biophys. J.* **97,** 101–109 (2009).

13. Gaffield, M. A. & Betz, W. J. Imaging synaptic vesicle exocytosis and endocytosis with FM dyes. *Nat. Protoc.* **1,** 2916–2921 (2006).

14. Haugland, R. P., Gregory, J., Spence, M. T. Z. & Johnson, I. D. *Handbook of fluorescent probes and research products*. (Molecular Probes, 2002). at <http://books.google.com/books?id=HagKAQAAMAAJ>

15. Betz, W. J., Mao, F. & Smith, C. B. Imaging exocytosis and endocytosis. *Curr. Opin. Neurobiol.* **6,** 365–371 (1996).

16. Fernández-Busnadiego, R. *et al.* Quantitative analysis of the native presynaptic cytomatrix by cryoelectron tomography. *J. Cell Biol.* **188,** 145–156 (2010).

17. Moore, B. A., Robinson, H. H. & Xu, Z. The crystal structure of mouse Exo70 reveals unique features of the mammalian exocyst. *J. Mol. Biol.* **371,** 410–421 (2007).

18. Sivaram, M. V. S., Furgason, M. L. M., Brewer, D. N. & Munson, M. The structure of the exocyst subunit Sec6p defines a conserved architecture with diverse roles. *Nat. Struct. Mol. Biol.* **13,** 555–556 (2006).

CHAPTER 5

AFM/TIRF FORCE CLAMP MEASUREMENTS OF NEUROSECRETORY VESICLE TETHERS REVEAL CHARACTERISTIC UNFOLDING STEPS

5.1 Abstract

Nanomechanical properties of secretory vesicle-plasma membrane tethers were measured by combined AFM force clamp and TIRF microscopy on membrane sheets from PC12 cells expressing the vesicle marker ANF-eGFP. Tethers were more easily unfolded in the presence of GTPγS, as indicated by a higher frequency of short tether extension events. A mean length for the short extension events of ~7 nm was identified, consistent with extension lengths expected from unfolding of a single alpha helix of the exocyst complex. The frequency of these extension events was markedly increased when a fluorescent vesicle was identified at the cantilever tip, indicating that the method reveals specifically the biomechanical properties of physiological vesicle-plasma membrane tethers. The stepwise tether extension events observed with this method are consistent with progressive unfolding of helical domains of the exocyst complex.

5.2 Introduction

The fusion of secretory vesicles with the plasma membrane occurs from a tethered state, in which the vesicles are associated with the plasma membrane via long-range interactions that do not require the cytoskeleton[1]. The identities of the proteins that form the physical tether are not known[2].

Vesicle-plasma membrane tethering is followed by docking, priming, and finally vesicle fusion. The precise distinction between these steps has not been clear and consistent in the literature, due in part to limitations of electron microscopic studies[3]. One suggestion is that the vesicle and target membrane are held together within >25 nm in the tethered state, and 5 – 10 nm in the docked state[4]. Additionally, the docked state is widely thought to involve trans-pairing of Soluble N-ethylmaleimide sensitive factor (NSF) Attachment Protein Receptors (SNAREs)[5,6], which can only begin to form when the vesicle-plasma membrane distance is below 8 nm[7]. The SNARE proteins in the vesicle and plasma membrane form a coiled coil, and unzippering of the SNARE complex using optical tweezers results in ~8.3 nm extension[8]. Therefore, we consider docking to be a state that involves trans-pairing of SNAREs, while tethering precedes trans-pairing of SNAREs. The primed state is thought to involve partial SNARE complex assembly[1] and making the vesicle readily releasable[3].

Multiple protein complexes have been implicated in exocytosis. Among them are long coiled-coil proteins and multi-subunit tethering complexes (MTCs)[1]. Many MTCs contain CATCHR (Complex Associated with Tethering Containing Helical Rods) domains, characterized by an extended rod-like structure composed of helical bundles[1,9]. These CATCHR domains promote an elongated structure and mediate interactions with other proteins, such as GTPases. Among the CATCHR proteins that have been implicated in exocytosis are the exocyst complex, Conserved Oligomeric Golgi (COG) complex, Dsl1 complex, Golgi-associated Retrograde Protein (GARP) complex, Calcium-dependent Activator Protein for Secretion (CAPS), Munc13, and

the class V myosin Myo2. The HOPS (Homotypic Fusion and Vacuole Protein Sorting) complex, which likely provides the tethering required for homotypic fusion between large organelles, lacks CATCHR domains. The exocyst complex is a leading candidate as the physical tether between neurosecretory vesicles and the plasma membrane. Many GTP-binding proteins, such as members of the Rab family, have also been implicated in tethering[1]. Some examples of Rab proteins acting on tethering factors are: Sec4 acting on the exocyst, Ypt7 acting on HOPS, Rab1 acting on p115, and Rab5 acting on EEA1[3].

The method described in chapter 4 was used to directly apply a force clamp to secretory vesicles tethered to plasma membrane sheets[10,11]. In the presence of GTPγS, a distribution of tether extension steps around ~7 nm was observed, consistent with sequential unfolding of helical domains as found in members of the CATCHR family.

5.3 Methods

5.3.1 Data Selection for Analysis

Data were collected using the method described in chapter 4. In some experiments, the buffer was supplemented with 100 μM GTPγS (11 110 349 001, Roche Diagnostics, Indianapolis, IN), obtained as a gift from Dr. Richard Cerione's lab at Cornell University. As described in section 4.3.8, a small number (Table 5.1) of segments with F outside of the range of -200 – 1000 pN were removed, (where a negative F value represented a push force). To eliminate the segments with least reliable measurements of F while retaining the majority, segments with $\sigma_F > 200$ pN were also removed.

Tether extension or tether dissociation events were not expected to occur at a push force, so all segments in the range of -200 – 0 pN with an F error <200 pN were checked for either R events or FC events. In total, 10 out of 152 segments in that range had events. Of those 10 segments, the one with the highest F magnitude had F = – 31.71 pN. The smallest error in all the segments was 52.15 pN, and the remaining 9 segments had error >160 pN. Thus, there is no significant evidence that any tether extension events occurred at push forces, and segments with F < 0 pN were removed from the analysis. Table 5.1 shows the number of total segments included in the data set after each of the above steps.

Table 5.1. Number of segments remaining in the data set after removal of different segment types.

Segment Type Removed	Number of segments left afterwards
Did not reach target F value	1229
F > 1000 pN	1146
F < -200 pN	1102
σ_F > 200 pN	793
F < 0 pN	641

5.3.2 Statistics

The 68% confidence intervals of the binomial distribution were calculated using the program R's "binom.confint" command to execute the Pearson-Klopper method. The Pearson correlation coefficient was also calculated using R

(http://www.r-project.org). R's "sample" command was used to choose random segments for analysis.

5.4 Results

5.4.1 Multiple Types of Tether Extensions

Section 4.4.3 described a strong correlation between the tether extension of an event as measured by the AFM servo and the change in the intensity of the TIRF excitation of the vesicle, confirming that the measured extension corresponded with extension of the vesicle-plasma membrane tether. Although such a detailed analysis was rarely possible, a large number of events showed a fluorescent vesicle at the AFM tip that dimmed associated with AFM tip retraction. For analysis, if some fluorescence change was seen in a 3 pixel by 3 pixel region near the cantilever tip during a force clamp experiment, that recording was labeled as +ΔFluor, indicating the presence of a fluorescent vesicle. Otherwise, the experiment was labeled as –ΔFluor. In the latter category, a direct AFM tip-plasma membrane interaction may have occurred that did not involve a vesicle or the vesicle fluorescence may have been too dim to be detected.

For analysis, the events were separated into different types, as illustrated in Fig. 5.1. Type FC (force clamp) events occurred during the force clamp, after the V_{defl} setpoint for the segment was reached. Type R (rapid) events occurred before the setpoint V_{defl} for the segment was reached. They were characterized by noticeable transients in the deflection trace. Type F (full dissociation) events were characterized

by a sudden increase in V_{defl}, after which there was no evidence of a pull force. These events represented a full dissociation of the cantilever tip from the surface.

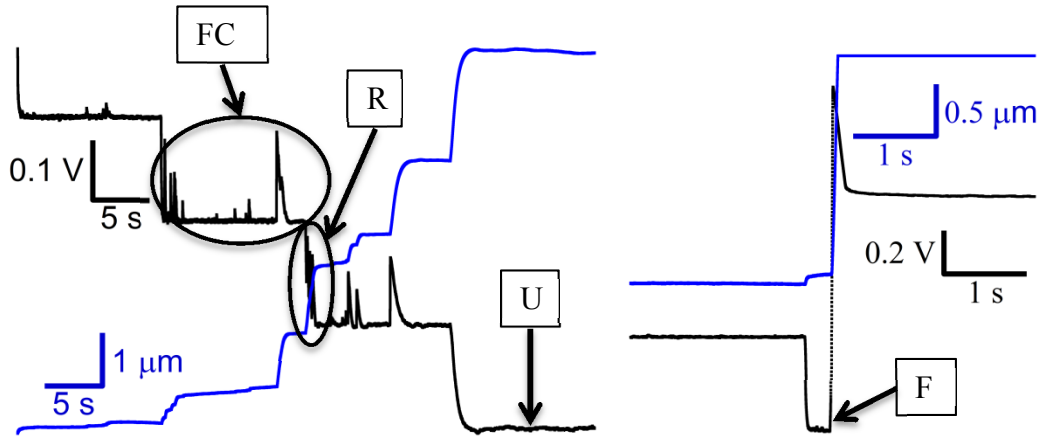

Figure 5.1. Classification of event and segment types. Traces show V_{defl} (black) and z_{servo} (blue). FC (force clamp) events occur after V_{defl} setpoint is reached. R (rapid) events occur before the V_{defl} setpoint is reached. F events occur when the tip dissociates fully from the surface. U (uncertain) segments contain no evidence that a pulling force is being applied to the cantilever tip.

Pull force segments were classified by visual inspection of the traces according to the types of events they contained. Since events of different types could occur in a single segment, segment classification represented all types observed. If the cantilever deflection, V_{defl}, did not reach the target setpoint deflection, this indicated that the tip was not in contact with the surface, and the segment was discarded. A segment was labeled as type U (uncertain) if the cantilever tip was not in contact with or pulling on anything during that segment (Fig. 5.1, last segment). In such cases, the V_{defl} signal could still differ from the baseline V_{defl} because V_{defl} changed for large z_{servo} values in the absence of a force bending the cantilever. However, U segments could be clearly identified by the following criteria: no events after the setpoint V_{defl} was reached, all following segments showed no events of any type, and all V_{defl} increases during or

after the segment in question were accompanied by increases in z of approximately 1 μm or more. 81 of the 641 segments were of type U, and these segments were excluded from the analysis.

5.4.2 More Segments Show Tether Extension Events in the Presence of GTPγS

Vesicle-plasma membrane tethering is regulated by GTP-binding proteins. Therefore, the occurrence and properties of tether extension events were compared between experiments in the presence and absence of 100 μM GTPγS. The proportion of segments that contained FC events (P_{FC}) as a function of time after cell lysis (t_{lysis}) (Fig. 5.2) shows that in the absence of GTPγS, P_{FC} increased significantly, as determined by unweighted linear regression, up to $t_{lysis} \approx 60$ min, eventually reaching $P_{FC} \approx 0.6$. This increase in frequency of tether extension or tether dissociation events indicates that tether stability decreased over time, which is consistent with previous observations of a gradual rundown in the ability of membrane sheets to support exocytosis after cell lysis[10,11]. In the presence of GTPγS, P_{FC} started at ~0.6 followed by a much weaker increase, suggesting that the presence of GTPγS rapidly enabled the tether extension events.

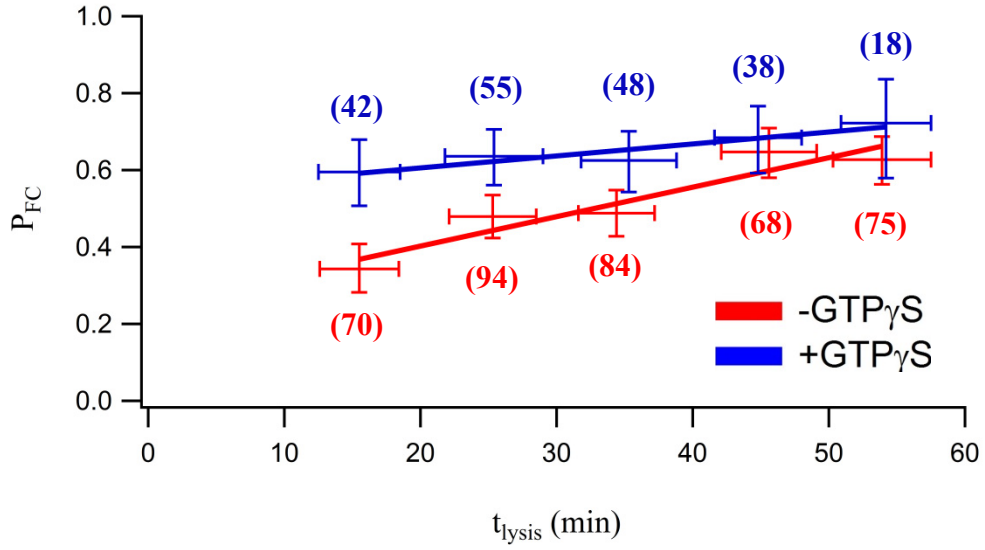

Figure 5.2. The proportion of segments showing force clamp events at different times since cell lysis. The proportion of segments showing events increases with t_{lysis} at a rate of ~7.7×10^{-3} min^{-1} in the absence of GTPγS, but starts high and increases at a much lower rate of ~3.1×10^{-3} min^{-1} in the presence of GTPγS. For each segment, time after cell lysis was determined and sorted in 10 min wide bins. Data points and error bars indicate for each bin mean and sd of t_{lysis} and mean P_{FC} with 68% confidence intervals for the binomial distributions. The numbers in parentheses are the number of segments included in each bin.

P_{FC} also increased as pull force increased, up to $F \approx 500$ pN (Fig. 5.3). Where $F < 300$ pN, P_{FC} was slightly higher in the presence of GTPγS, indicating that GTPγS was particularly effective at enabling tether extension events under small pull forces. For all segments included in the analysis, Pearson's correlation coefficient between t_{lysis} and F was calculated. The correlation was found to be 0.014, suggesting no significant correlation. Therefore, t_{lysis} and F were treated as independent variables.

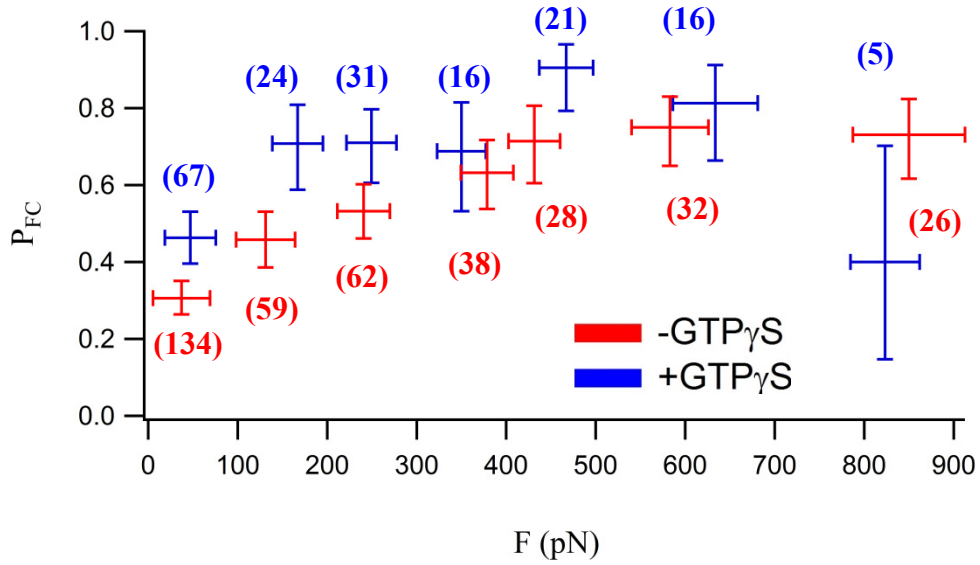

Figure 5.3. The proportion of segments showing force clamp events at different pull forces. The proportion of segments showing events increases with *F* both in the presence and absence of GTPγS, but is slightly starts higher in the presence of GTPγS where $F < 300$ pN. The segments were sorted into bins based on *F*. Data points and error bars indicate for each bin weighted mean and sd of *F*, and mean P_{FC} with 68% confidence intervals for the binomial distributions. The numbers in parentheses are the number of segments included in each bin.

5.4.3 GTPγS Increases Frequency of Short Tether Extension Events

Individual tether extension events were analyzed in more detail for a subset of randomly chosen segments comparing four experimental conditions: +GTPγS and +ΔFluor, +GTPγS and –ΔFluor, -GTPγS and +ΔFluor, and –GTPγS and –ΔFluor. Segments were chosen such that the total pull time included in the chosen segments from each of the four conditions was similar (221 s for +GTPγS and+ΔFluor, 229 s for +GTPγS and –ΔFluor, 238 s for –GTPγS and +ΔFluor, 200 s for –GTPγS and –ΔFluor). Pull time referred to the time elapsed between the pull force initially

reaching the setpoint (after any R events) and the end of the segment or the occurrence of an F event.

Each of the chosen segments was then inspected for FC events. For each event, AFM servo position change (Δz) was measured (Fig. 5.4). To correct for background drift in z, a baseline was fit to the portion of the z trace before the event occurred and projected to after the end of the event. Δz was then taken as the difference between the measured z value and the projected z value.

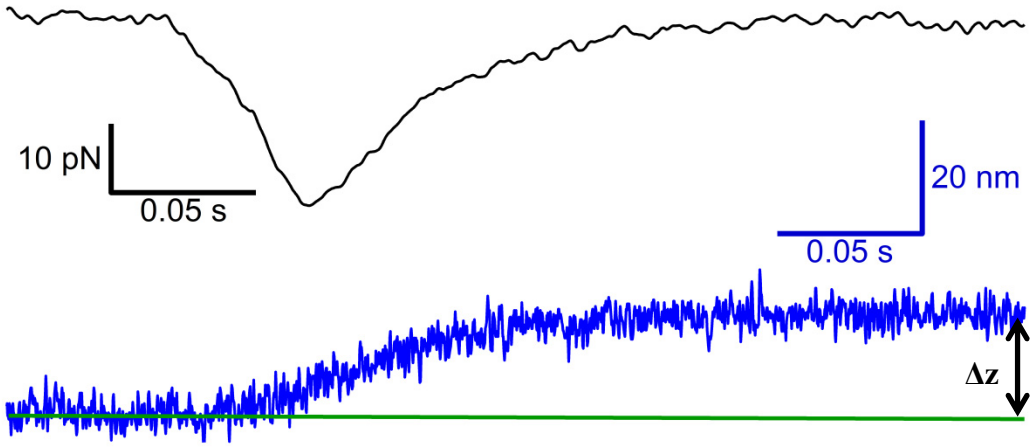

Figure 5.4. Measurement of event extension length. The event is characterized by a transient decrease in pull force (black trace) determined from the V_{defl} change and a stepwise increase in z (blue trace). Note that pull force has opposite sign to V_{defl}. The green line is a projection of the baseline of z from before the event to after, and the difference between the projected and observed z values is Δz, in this case 18 nm.

Fig. 5.5 shows histograms of Δz values for all analyzed events. A very large range of Δz was observed (Panel A), but most extensions were 50 nm or less, with an apparent peak at a Δz of 5 – 10 nm (Panel B.) To distinguish between the primary cluster of events that occurred at small Δz values and the widely scattered selection of

events at larger Δz values, extension events were split into those with Δz < 50 nm (S or short events), and those with Δz >50 nm (E or extended events).

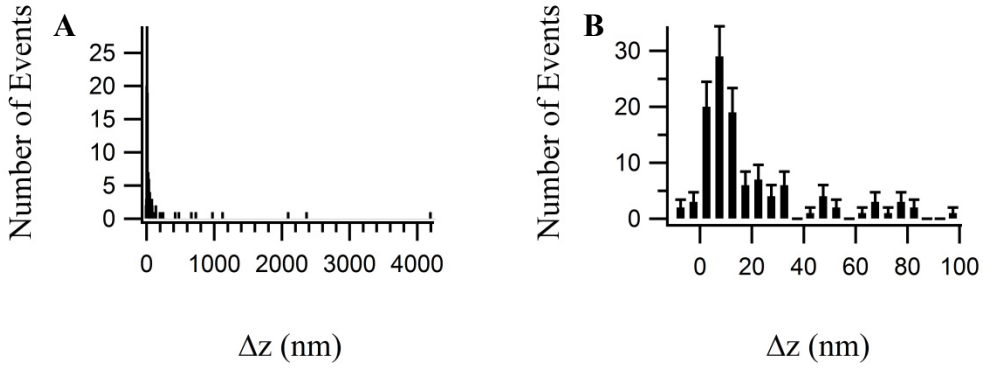

Figure 5.5. Distribution of tether extensions. Panel A: The full histogram of Δz values for all extension events. Panel B: The histogram of Δz values up to 100 nm. The tops of the black bars indicate the number of events in each bin, and the error bars are the square root of the number of events.

Some events did not consist of a single peak followed by an exponential decay, but appeared to consist of multiple transients that occurred so rapidly that they overlapped. Those events were classified as C_S (complex short) events (extension <50 nm) or C_E (complex extended) events (extension >50 nm). Fig. 5.6 shows examples of the different event types, and Table 5.2 shows the final classification of constant force events.

TABLE 5.2. Classification of constant *F* events.

Classification	Δz	Appearance in Force Trace
S (short)	<50 nm	Single Peak Transient
E (extended)	>50 nm	Single Peak Transient
C_S (complex short)	<50 nm	Complex Transient
C_E (complex extended)	>50 nm	Complex Transient

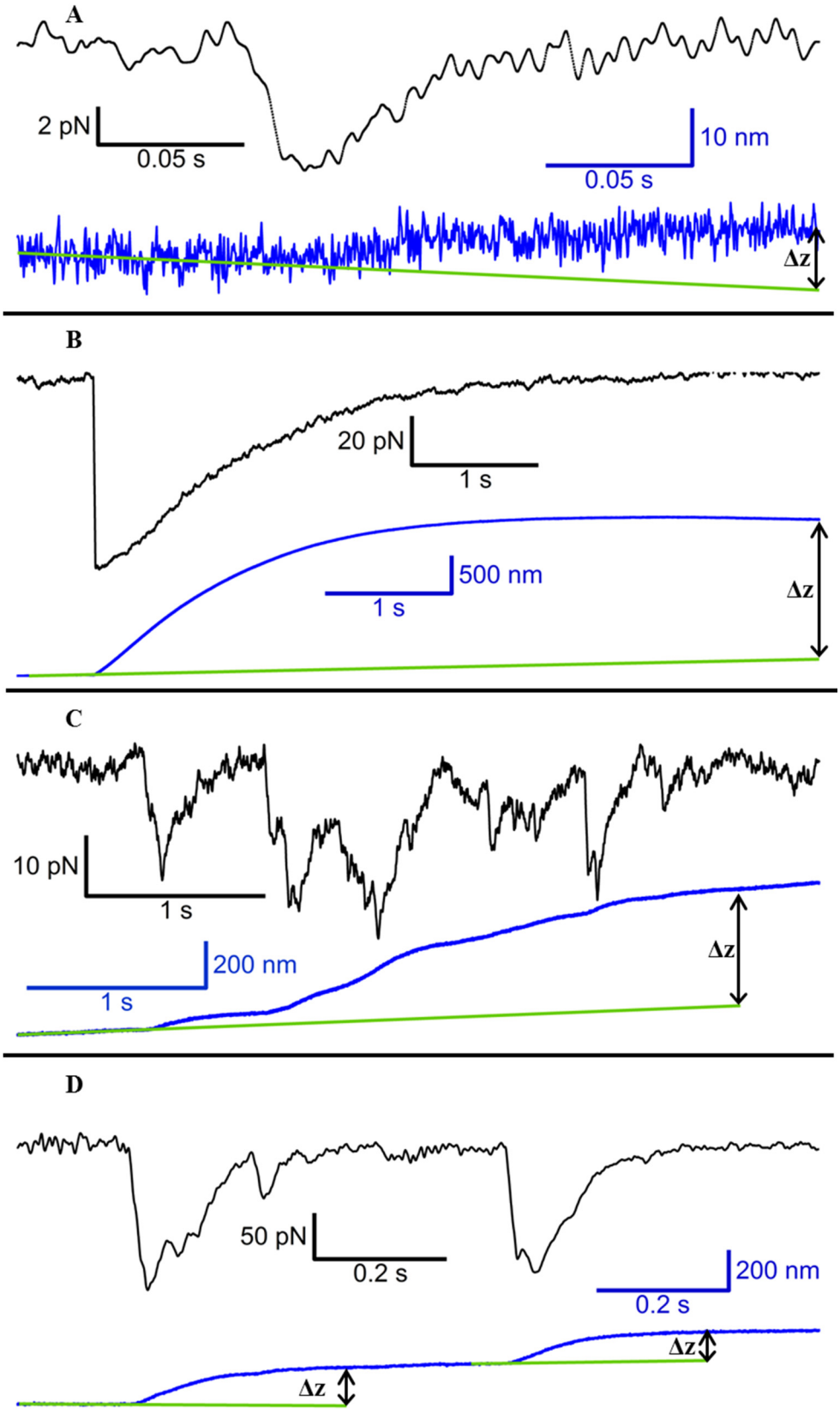
A
2 pN
0.05 s
10 nm
0.05 s
Δz
B
20 pN
1 s
500 nm
1 s
Δz
C
10 pN
1 s
200 nm
1 s
Δz
D
50 pN
0.2 s
200 nm
0.2 s
Δz
Δz

Figure 5.6. Examples of S, E, and C events. A: S event, with Δz 11 nm. B: E event, with Δz 1839 nm. S and E events decay smoothly enough to be fit well by an exponential. C: C event with many small, overlapping force transients and tether extensions, resulting in total Δz 501 nm. D: Two C events with multiple peaks in the force trace, the first with Δz 193 nm, the second with Δz 142 nm. These events may consist of multiple events that overlap, resulting in the multiple peaks.

Fig. 5.7 A, B shows histograms of Δz values for S and C_S events from +ΔFluor segments, i.e. events that occurred during a force clamp experiment in which a fluorescent vesicle was observed to be pulled by the cantilever tip, while panels C and D show events from –ΔFluor segments (no observable vesicle). Panels A and C show results obtained in the presence of GTPγS, and panels B and D in its absence. In the presence of GTPγS (Fig. 5.7 A,C), the histograms show a clear peak that could be fitted well by a Gaussian. With +GTPγS and +ΔFluor, the Gaussian peaked at an extension of 7.3±0.4 nm and had standard deviation 3.9±0.5 nm. With +GTPγS and –ΔFluor, the Gaussian peaked at 9.2±0.7 nm and had standard deviation 5.5±0.7 nm. This indicates that GTPγS specifically enabled tether extension events <50 nm, with mean extension of ~7 nm. The frequency of tether extension events <50 nm in the presence of GTPγS was much higher in recordings where a fluorescent vesicle was attached to the AFM tip (Fig. 5.7E) than in measurements where no fluorescent vesicle was detected. These results indicate that the activation of short tether extension events is specific for vesicle-plasma membrane tethers. There was no difference in the frequency of long (>50 nm) tether extension events among the different experimental conditions.

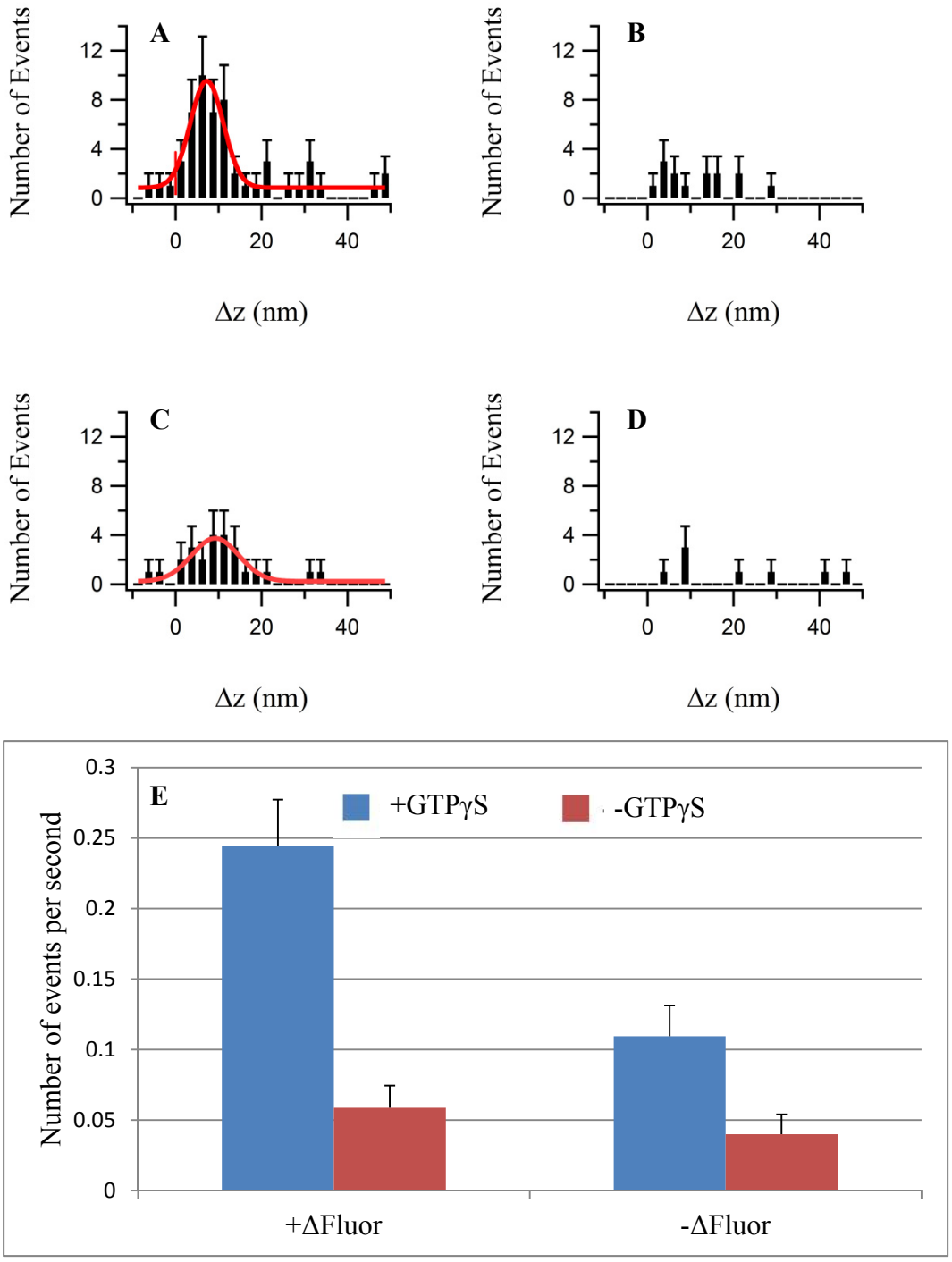

Figure 5.7. Distribution of tether extension lengths. Histograms of Δz are shown for (A) +GTPγS and +ΔFluor, (B) –GTPγS and +ΔFluor, (C) +GTPγS and –ΔFluor, and (D) –GTPγS and –ΔFluor. Negative values are possible because of fluctuations in the background. Error bars are the square root of the number of events in the bin. The

red lines in panels A and C are Gaussian fits to the histograms that reveal a peak at ~7 nm. Panel E shows the dependence of the frequency of tether extension events <50 nm under force clamp on the presence of GTPγS and ΔFluor. In experiments with +GTPγS or +ΔFluor, the frequency of extension events is much larger and the events cluster around smaller extension values.

5.5 Discussion

Fusion of secretory vesicles with the plasma membrane is preceded by various steps including tethering, docking, and priming[1]. Long tethers (>5 nm) providing a mechanical link between secretory vesicles and the plasma membrane have been observed by electron microscopy[12], but their mechanical properties are unknown. Here, the approach developed in chapter 4 was used to perform AFM force clamp measurements on secretory vesicles of ANF-eGFP expressing PC12 cells associated with plasma membrane sheets that revealed stepwise tether extension events. Simultaneous TIRF imaging of the GFP-labeled vesicles allowed direct detection of vesicle displacement during tether extension induced by mechanical force pulling on the vesicle.

When pulling forces in the range of a few hundred pN were applied, sequential tether extension steps were typically observed. In force clamp experiments in which a fluorescent vesicle was visible at the AFM tip, GTPγS produced a ~5-fold increase in the frequency of short tether extension events with a Gaussian distribution of 7.3±3.9 nm. The frequency of such events was much lower when a fluorescent vesicle was not detectable at the AFM tip. These results indicate that the short tether extension events were specifically extensions of the vesicle-plasma membrane tether. In contrast, the frequency of longer tether extension events (>50 nm) was independent of the presence

of a fluorescent vesicle or GTPγS, suggesting that they may reflect other interactions of the AFM tip with the cytoplasmic face of the plasma membrane.

The mechanics of secretory vesicle-plasma membrane tethers revealed by these experiments support the hypothesis that the exocyst complex may be the physical link in the tethered state. The exocyst complex consists of 8 subunits: Sec3, Sec5, Sec6, Sec8, Sec10, Sec15, Exo70, and Exo84[1]. Exo84 was in fact first identified in PC12 cells[13]. The exocyst complex has been shown to function after neurosecretory vesicles have been delivered to exocytic sites, but prior to formation of SNARE complexes[14], which suggests a role of the exocyst during the tethering phase of exocytosis. The exocyst also determines when and where vesicles are tethered[14]. The components Exo70 and Sec3 are associated with the plasma membrane, and Sec3 is localized to exocytic sites[15], while the remaining subunits are bound to the vesicle. These findings had led to the hypothesis that assembly of the full complex could form the physical tether[1,16]. The structures of the four domains of mammalian Exo74[17] and the Sec6 C-terminal domain[18] have been studied in detail. They consist of helical bundles with α-helices ~25–40 amino acids in length. Assuming an unfolded contour length of 0.365 nm per amino acid[8], and noting that the rise per amino acid of a folded α-helix is 0.15 nm, we expect an extension of 0.215 nm per residue during unfolding or 5.4 – 8.6 nm to result from the unfolding of a single α-helix. These estimates are in excellent agreement with the mean length of 7±4 nm we observed for vesicle-plasma membrane tether extensions in the presence of GTPγS. The relatively large standard deviations of the Gaussian fits are consistent with the extension events resulting from unfolding of several different helices of varying lengths. It is possible that some events represent

simultaneous unfolding of multiple domains. Even the existence of multiple short vesicle tethers has been observed associated with vesicles <5 nm from the plasma membrane[12].

Fig. 4.8 shows a total extension length >3 μm from the beginning of force clamp application until the last extension event in segment 3, which raises the question whether such long extension lengths could be accounted for by unfolding of a single exocyst complex between the vesicle and the plasma membrane. The sequences of the 8 subunits of the rat exocyst complex are available on the NIH Protein database. All subunits are large proteins composed of 653 (exo70) to 975 (sec8) amino acids and the total number of residues of all subunits is 6,216. With an unfolded contour length of 0.365 nm per amino acid, this would give a total unfolded length of ~2.3 μm. While this value approaches the total tether extensions obtained in our experiments, it is somewhat smaller, and it seems unlikely that the unfolding of all the exocyst components could produce such a fully extended chain. It therefore appears that other proteins must be involved to account for the large extensions. One possibility is actin, as actin is involved in many steps of exocytosis, including an interaction between Myo2, the yeast homologue of Myosin Va, and the exocyst complex in yeast[19]. The role of actin could be investigated in force clamp experiments on membrane sheets where cortical actin is disrupted using cytochalasin or latrunculin.

A central finding of our study is a marked increase in the frequency of the ~7 nm tether extension events in the presence of GTPγS, indicating that GTPγS destabilizes tethers and facilitates tether unfolding. This result further supports the conclusion that the ~7 nm events are specific to vesicle-membrane tethers, due to the

multiple roles of GTP-binding proteins in the tethering process, and in particular in the function of the exocyst. The GTP-binding protein sec4p, which is present on secretory vesicles[20], is required for the exocyst complex to fully assemble[21]. Subunit Sec15p binds preferentially to the GTP-bound form of sec4p[21]. When the mammalian ortholog of sec4p, Rab3a[22], is locked in either the GTP-bound or the GDP-bound state in chromaffin cells, the number of vesicles within 100 nm of the plasma membrane decreases, while the number of vesicles found at distances >100 nm from the membrane is not affected[23]. The presence of GTPγS interferes with GTP-GDP cycling, and is therefore expected to interfere with tethering, and potentially to disrupt the fully assembled state of the exocyst, facilitating tether extensions. Additionally, interactions of Exo70 and Sec3 with GTPases from the Rho and cdc42 family are involved in recruitment of the exocyst complex to the plasma membrane[1], and TC10 binds preferentially to the GTP-bound form of TC10[24].

A 5-fold increase in the frequency of ~7 nm tether extension events by GTPγS was obtained in measurements with a fluorescent vesicle attached to the AFM tip, indicating that these events were associated specifically with vesicle-plasma membrane interactions. However, a smaller increase in the frequency of such events was still seen when no fluorescent vesicle was detectable. One possible explanation for this is that in some of these experiments a vesicle was being pulled on by the cantilever tip, but the vesicle was too high above the membrane surface to be illuminated by the TIRF evanescent wave or the fluorescence labeling of the vesicle was too dim, or that the vesicle was disrupted by the AFM tip but its membrane still attached to the AFM tip and tethered to the plasma membrane. Fig. 4.8 shows many

events that occurred after the vesicle was already pulled out of the evanescent wave. If the vesicle began the run already above the evanescent wave, no change in fluorescence would have been observed, and the experiment would have been labeled as –ΔFluor. Alternatively, some of the ~7 nm extension events may have been due to tethers other than the vesicle-plasma membrane tether. GARP, a tethering complex involved in traffic from the endosomes to the trans-Golgi network, has CATCHR morphology, suggesting that tethering mechanisms may be similar for the various membrane trafficking pathways in the cell[25].

Optical trapping experiments in which a half zippered state of the SNARE complex was stabilized showed that unzippering of the N-terminal portion of the SNARE complex results in an extension of 8.3 nm[8]. Since only the N-terminal portion of the SNARE complex is thought to be zippered in the trans state[26], this suggests the possibility that ~7 nm extension events could be due to SNARE complex unzippering. However, the existence of a stable trans state is still being debated[26]. Additionally, unzippering of the SNARE complex cannot account for extension events that occur >10 nm from the plasma membrane. If the vesicle were only linked to the membrane by the SNARE complex, it would dissociate completely once a separation of ~ 15 nm from the membrane occurred.

The experiments described here establish a highly versatile method of directly measuring the mechanical properties of vesicle-plasma membrane tethers and their regulation. In future experiments, it could be tested if tetanus toxin, which cleaves synaptobrevin, facilitates tether extensions, which would support the existence of trans-SNARE complexes in the docked state. It has been reported that vesicle

tethering still occurs after tetanus toxin treatment, but the duration of tethering events becomes shorter[27]. AFM force clamp experiments on RIM1α knock-out cells could reveal whether the knock-out has a tether destabilizing effect similar to GTPγS. In RIM1α knock-out synapses, the fraction of tethers <5 nm in length decreased[2], possibly representing a disruption of stable tethering that prevents docking. Also, measurement of the extension of purified exocyst subunits, such as Exo70 and Sec6, under AFM force clamp would allow comparison with the stepwise extensions of vesicle-plasma membrane tethers observed in the present experiments and show whether exocyst subunits share the mechanical properties of the vesicle-plasma membrane tether.

REFERENCES

1. James, D. J. & Martin, T. F. J. CAPS and Munc13: CATCHRs that SNARE Vesicles. *Front. Endocrinol. (Lausanne).* **4,** 187 (2013).

2. Fernández-Busnadiego, R. *et al.* Cryo-electron tomography reveals a critical role of RIM1α in synaptic vesicle tethering. *J. Cell Biol.* **201,** 725–740 (2013).

3. Burgoyne, R. D. & Morgan, A. Secretory granule exocytosis. *Physiol. Rev.* **83,** 581–632 (2003).

4. Pfeffer, S. R. Transport-vesicle targeting: tethers before SNAREs. *Nat. Cell Biol.* **1,** 17–22 (1999).

5. Pfeffer, S. Vesicle tethering factors united. *Mol. Cell* **8,** 729–730 (2001).

6. Cai, H., Reinisch, K. & Ferro-Novick, S. Coats, tethers, Rabs, and SNAREs work together to mediate the intracellular destination of a transport vesicle. *Dev. Cell* **12,** 671–682 (2007).

7. Li, F. *et al.* Energetics and dynamics of SNAREpin folding across lipid bilayers. *Nat. Struct. Mol. Biol.* **14,** 890–896 (2007).

8. Gao, Y. *et al.* Single reconstituted neuronal SNARE complexes zipper in three distinct stages. *Science* **337,** 1340–1343 (2012).

9. Yu, I.-M. & Hughson, F. M. Tethering factors as organizers of intracellular vesicular traffic. *Annu. Rev. Cell Dev. Biol.* **26,** 137–156 (2010).

10. Avery, J. *et al.* A cell-free system for regulated exocytosis in PC12 cells. *J. Cell Biol.* **148,** 317–324 (2000).

11. Lang, T. Imaging Ca2+-triggered exocytosis of single secretory granules on plasma membrane lawns from neuroendocrine cells. *Methods Mol. Biol.* **440,** 51–59 (2008).

12. Fernández-Busnadiego, R. *et al.* Quantitative analysis of the native presynaptic cytomatrix by cryoelectron tomography. *J. Cell Biol.* **188,** 145–156 (2010).

13. Kee, Y. *et al.* Subunit structure of the mammalian exocyst complex. *Proc. Natl. Acad. Sci. U. S. A.* **94,** 14438–14443 (1997).

14. Munson, M. & Novick, P. The exocyst defrocked, a framework of rods revealed. *Nat. Struct. Mol. Biol.* **13,** 577–581 (2006).

15. Grote, E., Carr, C. M. & Novick, P. J. Ordering the final events in yeast exocytosis. *J. Cell Biol.* **151,** 439–451 (2000).

16. Boyd, C., Hughes, T., Pypaert, M. & Novick, P. Vesicles carry most exocyst subunits to exocytic sites marked by the remaining two subunits, Sec3p and Exo70p. *J. Cell Biol.* **167,** 889–901 (2004).

17. Moore, B. A., Robinson, H. H. & Xu, Z. The crystal structure of mouse Exo70 reveals unique features of the mammalian exocyst. *J. Mol. Biol.* **371,** 410–421 (2007).

18. Sivaram, M. V. S., Furgason, M. L. M., Brewer, D. N. & Munson, M. The structure of the exocyst subunit Sec6p defines a conserved architecture with diverse roles. *Nat. Struct. Mol. Biol.* **13,** 555–556 (2006).

19. Porat-Shliom, N., Milberg, O., Masedunskas, A. & Weigert, R. Multiple roles for the actin cytoskeleton during regulated exocytosis. *Cell. Mol. Life Sci.* **70,** 2099–2121 (2013).

20. Whyte, J. R. C. & Munro, S. Vesicle tethering complexes in membrane traffic. *J. Cell Sci.* **115,** 2627–2637 (2002).

21. Guo, W., Roth, D., Walch-Solimena, C. & Novick, P. The exocyst is an effector for Sec4p, targeting secretory vesicles to sites of exocytosis. *EMBO J.* **18,** 1071–1080 (1999).

22. Sato, Y., Fukai, S., Ishitani, R. & Nureki, O. Crystal structure of the Sec4p.Sec2p complex in the nucleotide exchanging intermediate state. *Proc. Natl. Acad. Sci. U. S. A.* **104,** 8305–8310 (2007).

23. Van Weering, J. R. T., Toonen, R. F. & Verhage, M. The role of Rab3a in secretory vesicle docking requires association/dissociation of guanidine phosphates and Munc18-1. *PLoS One* **2,** e616 (2007).

24. Inoue, M., Chang, L., Hwang, J., Chiang, S.-H. & Saltiel, A. R. The exocyst complex is required for targeting of Glut4 to the plasma membrane by insulin. *Nature* **422,** 629–633 (2003).

25. Vasan, N., Hutagalung, A., Novick, P. & Reinisch, K. M. Structure of a C-terminal fragment of its Vps53 subunit suggests similarity of Golgi-associated retrograde protein (GARP) complex to a family of tethering complexes. *Proc. Natl. Acad. Sci. U. S. A.* **107,** 14176–14181 (2010).

26. Jahn, R. & Fasshauer, D. Molecular machines governing exocytosis of synaptic vesicles. *Nature* **490,** 201–207 (2012).

27. Johns, L. M., Levitan, E. S., Shelden, E. A., Holz, R. W. & Axelrod, D. Restriction of Secretory Granule Motion near the Plasma Membrane of Chromaffin Cells. *J. Cell Biol.* **153,** 177–190 (2001).

CHAPTER 6

CONCLUSIONS AND FUTURE DIRECTIONS

Although exocytosis has been widely studied, much remains to be discovered. In particular, the identities and mechanical properties of the tether than links a secretory vesicle with the target membrane during the tethering phase of exocytosis are not known. Application of pull forces to reconstituted or isolated proteins has revealed much about their mechanical and folding properties, but the typical single molecule approach is restricted to proteins whose identities are known. This work has expanded these methods to physiological vesicle-plasma membrane tethers, and has further developed a method of studying the mechanical properties of physiological vesicle-vesicle tethers. This has opened new possibilities to identify not only the mechanical and regulatory properties of the tethers, but also the identities of the proteins of which the tethers are made.

In chapter 3, a procedure to test for vesicle-vesicle fusion *in vitro* by measuring dye transfer between two vesicles in a dual optical trap was described. Horse eosinophil secretory vesicles were labeled with a fluorescent marker, and the fluorescence intensity per vesicle volume was quantified as the vesicle were brought into contact and bound to each other. Although the evidence was not conclusive for the presence or absence of vesicle-vesicle fusion, the precision of the intensity concentration measurements shows promise. Control experiments to measure photobleaching and spatial variations in excitation intensity could allow for more conclusive results.

In chapters 4 and 5, a procedure using a combined atomic force microscopy (AFM) and total internal reflection fluorescence (TIRF) microscopy approach to directly measure mechanical and regulatory properties of neurosecretory vesicle-plasma membrane tethers was developed, and used to identify a characteristic extension length of the tether under applied pull force. The frequency of tether extensions at the characteristic extension length was strongly dependent on whether a fluorescent vesicle was observed attached to the AFM tip, indicating that the measured extensions represented disruption the vesicle-plasma membrane tether. Comparison of the characteristic extension length with the expected extension due to unfolding of an α-helix identified the exocyst complex as a likely candidate for future single molecule pulling experiments, which would reveal whether the mechanical and regulatory properties of the exocyst match the properties of the physiological tether directly observed in these experiments. Additionally, the frequency of the characteristic extensions depended strongly on the presence or absence of GTPγS, consistent with the known roles of GTP-binding proteins in regulation of tethering interactions, specifically in the regulation of the exocyst.

The AFM/TIRF method developed here is highly versatile, and can be adapted for various specific experiments by modification of the system. For example, cleaving or genetically inhibiting specific proteins (e.g. cleaving synaptobrevin with tetanus toxin or genetically deleting RIM1α) can determine what, if any, role those proteins have in tethering.

Much can also still be done with the AFM/TIRF method using the data collected for the experiments here. Most of the identification and analysis of the

extensions observed in the force-clamp experiments was done manually. Due to the time-consuming nature of this analysis, much of the statistics relied on a randomly selected subset of the data. A sufficiently sophisticated algorithm could identify and measure the properties of the extension events automatically, greatly increasing the speed and reproducibility of the analysis. Similarly, a method to automatically identify vesicle intensity changes in the TIRF recordings could be implemented.

Finally, the analysis of specific events can be expanded beyond extension length. The transient peaks in the force traces accompanying extension events display a range of amplitudes and decay times. With a sufficiently sophisticated understanding of the physics of the AFM servo feedback, the properties of the force transients may shed light on the kinetics of the tether extensions.

Overall, these methods provide a new means of investigating the mechanics and identities of the proteins that form the vesicle-vesicle and secretory vesicle-plasma membrane tethers. AFM/TIRF experiments identified mechanical and regulatory properties of the vesicle-plasma membrane tethers. The AFM/TIRF method is highly versatile, opening the door to an exciting array of future discoveries in the study of the tethering stage of exocytosis.

APPENDIX

AFM Control Script

```
import picoscript
import time

picoscript.SetServoActive(False)
#Set setpoint control of servo to off, so servo position can be controlled directly.

picoscript.SetSpectroscopyOutput(4)
#Set the output of the spectroscopy segments to force setpoint, meaning that the
#spectroscopy segments will be controlled by force setpoint.

ZSensorSensitivity = (.76)*1e-6
#The z sensor sensitivity value, previously determined by calibration of the AFM
#scanner.

camoff = [0]*3
#Define an array of three zeros.

picoscript.SpectroscopySegmentClearAll()
#Clear all spectroscopy segments from previous experiments.
```

```
f = open('last_run.txt','w')
#Open a file to store data recorded by this script.

x = picoscript.GetStatusRawDefl()
ZSensor = picoscript.GetStatusZSensor()
y = ZSensorSensitivity*ZSensor
yi = y
t0 = time.clock()
#Store initial values of x = cantilever deflection, y and yi = initial z sensor value
#corrected for closed loop feedback, t0 = initial clock value.

print "Start the camera."
#Outputs a note to the user indicating that script is recoring and the camera imaging
#can be initialized.

while picoscript.GetStatusBNC() < 4:
    defl = picoscript.GetStatusRawDefl()
    t1=time.clock()-t0
    sens=picoscript.GetStatusZSensor()*ZSensorSensitivity
    t2=time.clock()-t0
    bnc=picoscript.GetStatusBNC()
    t3=time.clock()-t0
```

```
    print>>f, t1, defl, t2, sens, t3, bnc
#Records values of time, cantilever deflection , z sensor, and camera FIRE signal
#(BNC) until the FIRE signal exceeds 4V, indicating that the camera is exposing.

print "Camera on.  Beginning approach."
print>>f, "Camera on.  Beginning approach."
#Outputs a note to the  user indicating that the script has detected the camera
#exposing, and is beginning the approach to the surface.

while picoscript.GetStatusRawDefl() < x+.05:
    defl = picoscript.GetStatusRawDefl()
    t1=time.clock()-t0
    sens=picoscript.GetStatusZSensor()*ZSensorSensitivity
    t2=time.clock()-t0
    bnc=picoscript.GetStatusBNC()
    t3=time.clock()-t0
    y=y-6e-9
    picoscript.SetServoZDirect(y)
    print>>f, t1, defl, t2, sens, t3, bnc

while (yi-y) > 5e-8:
    yi = y
    x=picoscript.GetStatusRawDefl()
```

```
    while picoscript.GetStatusRawDefl() < x+.05:
        defl = picoscript.GetStatusRawDefl()
        t1=time.clock()-t0
        sens=picoscript.GetStatusZSensor()*ZSensorSensitivity
        t2=time.clock()-t0
        bnc=picoscript.GetStatusBNC()
        t3=time.clock()-t0
        y=y-6e-9
        picoscript.SetServoZDirect(y)
        print>>f, t1, defl, t2, sens, t3, bnc
#Continues data recording while stepping the cantilever closer to the surface in 6nm
#intervals.  Approach continues until cantilever deflection exceeds initial value (x) by
#0.05V.  This threshold must be exceeded twice within a 50 nm distance.

picoscript.SetServoSetpoint(defl)
picoscript.SetServoActive(True)
#Set the deflection setpoint to the current value, and turn the servo setpoint control
#back on, so current deflection will be maintained.

print "In contact.  Stop the camera and start the next camera acquisition."
print>>f, "In contact."
#Outputs a note to the user indicating that contact is established.  Allows the user to
#end the camera acquisition, save data, and begin a new acquisition.
```

```
while camoff[2]==0:
    defl = picoscript.GetStatusRawDefl()
    t1=time.clock()-t0
    sens=picoscript.GetStatusZSensor()*ZSensorSensitivity
    t2=time.clock()-t0
    bnc=picoscript.GetStatusBNC()
    t3=time.clock()-t0
    print>>f, t1, defl, t2, sens, t3, bnc
    if bnc < 1:
        if camoff[0]==1:
            if camoff[1]==1:
                camoff[2]=1
            else: camoff[1]=1
        else: camoff[0]=1
    elif camoff[0]==1: camoff = [0]*3
#Waits for the camera to stop exposing, as indicated by three consecutive FIRE values
#less than 1.  Three consecutive values are needed because the FIRE signal briefly
#drops to 0 between each frame, and the script must not recognize that brief downtime
#as a stop in the camera exposure.

print "Camera off."
print>>f, "Camera off."
```

```
while picoscript.GetStatusBNC() < 4:
    defl = picoscript.GetStatusRawDefl()
    t1=time.clock()-t0
    sens=picoscript.GetStatusZSensor()*ZSensorSensitivity
    t2=time.clock()-t0
    bnc=picoscript.GetStatusBNC()
    t3=time.clock()-t0
    print>>f, t1, defl, t2, sens, t3, bnc
#Waits for a new exposure to begin.

print "Begin force curve!"
print>>f, "Begin force curve!"
f.close()
#Data recording ends, and the data file is closed.

picoscript.SetSpectroscopySegment(0,0,defl-.2,0,0,0,0,True,False,False,False)
picoscript.SetSpectroscopySegment(1,0,defl-.2,12.5,62500,0,0,True,False,False,False)

picoscript.SetSpectroscopySegment(2,0,defl-.25,0,0,0,0,True,False,False,False)
picoscript.SetSpectroscopySegment(3,0,defl-
.25,12.5,62500,0,0,True,False,False,False)
```

```
picoscript.SetSpectroscopySegment(4,0,defl-.3,0,0,0,0,True,False,False,False)
picoscript.SetSpectroscopySegment(5,0,defl-.3,12.5,62500,0,0,True,False,False,False)

picoscript.SetSpectroscopySegment(6,0,defl-.35,0,0,0,0,True,False,False,False)
picoscript.SetSpectroscopySegment(7,0,defl-
.35,12.5,62500,0,0,True,False,False,False)

picoscript.SetSpectroscopySegment(8,2,defl-.35,0,0,0,0,True,False,False,False)

#Set up the spectroscopy segments.  The servo moves as quickly as possible to each
#new setpoint, then maintains it for 12.5s.  The target setpoint values are relative to
#the last recorded cantilever deflection, and are hard-coded into the script before each
#run.

picoscript.SpectroscopySweepStart()
#Initiate the spectroscopy segments.
picoscript.WaitForStatusSpectroscopySweeping(False)
#Wait until the spectroscopy segments are complete.

picoscript.SetServoActive(False)
#Turn the servo setpoint control back off, allowing direct position control.
picoscript.SetServoZDirect(y+5e-7)
```

```
#Move the servo to about 500nm above the surface, so it is out of contact but not too
#far away.
time.sleep(3)
print picoscript.GetStatusRawDefl()
print time.clock()-t0
#Wait 3 seconds for the cantilever to settle, then print final time and cantilever
deflection values.
```